Strong-coupling study of the pairing mechanism in pressurized $La_3Ni_2O_7$

Jia-Heng Ji,[1,*] Chen Lu,[2,*] Zhi-Yan Shao,[1,*] Zhiming Pan,[3,*] Fan Yang,[1,†] and Congjun Wu[4,5,6,7,‡]

[1]*School of Physics, Beijing Institute of Technology, Beijing 100081, China*

[2]*School of Physics and Hangzhou Key Laboratory of Quantum Matter, Hangzhou Normal University, Hangzhou 311121, China*

[3]*Department of Physics, Xiamen University, Xiamen 361005, Fujian, China*

[4]*New Cornerstone Science Laboratory, Department of Physics, School of Science, Westlake University, Hangzhou 310024, Zhejiang, China*

[5]*Institute for Theoretical Sciences, Westlake University, Hangzhou 310024, Zhejiang, China*

[6]*Key Laboratory for Quantum Materials of Zhejiang Province, School of Science, Westlake University, Hangzhou 310024, Zhejiang, China*

[7]*Institute of Natural Sciences, Westlake Institute for Advanced Study, Hangzhou 310024, Zhejiang, China*

(Received 20 May 2025; revised 27 October 2025; accepted 5 December 2025; published 22 December 2025)

Recently, the bilayer perovskite nickelate $La_3Ni_2O_7$ has been reported to exhibit high-temperature superconductivity near 80 K under a moderate pressure of about 14 GPa. To investigate the underlying pairing mechanism and symmetry in this complex system, we propose and analyze a mixed spin-1 and spin-$\frac{1}{2}$ bilayer t-J model in the strong-coupling regime. This model explicitly incorporates the crucial role of strong Hund's coupling, which favors the formation of local spin-triplet states from the two on-site E_g orbital electrons at half-filling. We further investigate the model using both slave-particle mean-field theory and the density matrix renormalization-group method. Our simulation results reveal that the dominant pairing channel is the interlayer one in the $3d_{x^2-y^2}$ orbital. Hund's coupling is shown to enhance superconductivity within a reasonable physical range. Moreover, electron doping strengthens superconductivity by increasing carrier density; in contrast, hole doping weakens superconductivity. These findings offer critical insights into the unconventional superconductivity of pressurized $La_3Ni_2O_7$ and underline the important role of orbital-selective behavior and Hund's rule.

DOI: 10.1103/f6sr-t6js

I. INTRODUCTION

The discovery of high-T_c superconductivity (SC) with critical temperature $T_c \approx 80$ K in the bilayer perovskite nickelate $La_3Ni_2O_7$ under pressure [1–10] has garnered widespread attention, both experimentally [11–41] and theoretically [42–103]. More recently, the observation of ambient-pressure SC with $T_c \approx 40$ K in thin-film samples has attracted further attention [104–111]. These findings highlight the potential of nickelates as a new platform for exploring unconventional superconductors, particularly as analogs to the extensively studied cuprates [112–117]. In cuprates, doping introduces holes into the oxygen $2p$ orbitals, which form Zhang-Rice singlets with localized $3d_{x^2-y^2}$ orbital spins in the Cu^{2+} ions [118]. The suppression of long-range antiferromagnetic (AFM) order under doping leads to d-wave SC [112,113]. A similar scenario has been proposed for infinite-layer nickelates such as $Nd_{1-x}Sr_xNiO_2$ [119–121]. However, $La_3Ni_2O_7$ presents a more complex challenge due to its bilayer structure, unusual orbital filling, and strong electron correlations. Moreover, the T_c of the thin film at ambient pressure is much lower than that of the pressurized bulk $La_3Ni_2O_7$. Therefore, it is still necessary to understand the high T_c above the boiling point of liquid nitrogen in pressurized bulk $La_3Ni_2O_7$ by studying its pairing mechanism.

Recent theoretical and experimental studies have indicated that pressurized $La_3Ni_2O_7$ exhibits remarkable orbital-selective strong-correlation effects: According to first-principles calculations based on density-functional theory (DFT), the low-energy physics near the Fermi level are dominated by Ni-$3d_{z^2}$ and Ni-$3d_{x^2-y^2}$ orbitals, with occupancies of approximately one-half and one-quarter, respectively [42,48–50,75–80]. A range of experiments have demonstrated the strongly correlated characteristic of the bilayer nickelate material [14,15,19–21,23,24,26,30]. For instance, optical measurements report a notable reduction in electron kinetic energy, indicating proximity to the Mott phase [21]; angle-resolved photoemission spectroscopy (ARPES) experiment reveals pronounced orbital-selective band renormalization [23]; a linear temperature dependence of resistivity points to "strange-metal" behavior [2]; and the transport measurements of resistivity and magnetoresistance confirm Kondo-like scattering [26]. Together, these findings suggest that $La_3Ni_2O_7$ under pressure may provide a novel platform for exploring the interplay between orbital selectivity, strong correlations, and Hund's coupling.

At present, the pairing mechanism in pressurized $La_3Ni_2O_7$ remains an open question due to its complex electronic nature [42,45–62,64–71,73–83,85,86,89–91,97,102]. A key issue among theoretical proposals is determining which orbitals are most relevant for the SC. Some perspectives suggest that the SC of pressurized

*These authors contributed equally to this work.
†Contact author: yangfan_blg@bit.edu.cn
‡Contact author: wucongjun@westlake.edu.cn

$La_3Ni_2O_7$ is significantly related to hybridization between the nearest-neighbor (NN) $3d_{z^2}$ and $3d_{x^2-y^2}$ orbitals [51–53,81–83,85,86,90], while others emphasize the critical role of Hund's coupling in driving the superconducting behavior [47,58,60,67,68,70,71,73,81,83,86,90,91,94]. There is also a possibility that both factors are involved.

In this work, we propose and study a mixed spin-1 and spin-$\frac{1}{2}$ bilayer E_g-orbital t-J model, incorporating the spin coupling among and between the two orbitals. This model establishes a strong-coupling framework for identifying the dominant pairing channel in the bilayer system, while explicitly linking Hund's rule to superconducting strength. We solve the ground-state properties using the slave-particle mean-field (SPMF) [113,122] and the density matrix renormalization-group (DMRG) [123,124] methods. The numerical results reveal a phase diagram where the dominant pairing occurs in the interlayer $3d_{x^2-y^2}$ orbitals. Hund's coupling J_H promotes SC pairing and attracts a few $3d_{z^2}$-orbital electrons to the $3d_{x^2-y^2}$ orbital. The effect of doping is further explored, where electron-doping will enhance the SC pairing.

The remainder of this paper is organized as follows. Section II introduces the effective strong-coupling t-J model Hamiltonian. Section III details the SPMF analysis and the pairing nature. Section IV presents the DMRG calculations. Finally, Sec. V summarizes our findings and provides concluding remarks.

II. EFFECTIVE BILAYER TWO-ORBITAL MODEL

The electronic characteristics of the bilayer $La_3Ni_2O_7$ under pressure are predominantly influenced by the $d_{x^2-y^2}$ and d_{z^2} orbitals within the NiO_2 planes, which are naively quarter-filling and half-filling, respectively. The $d_{x^2-y^2}$ orbital is primarily responsible for in-plane conduction and dominates the electronic states near the Fermi level, contributing to the metallic behavior observed in the normal state. On the other hand, the d_{z^2} orbital is more localized, with its lobes extending out of the NiO_2 planes, thereby mediating the interlayer coupling between adjacent NiO_2 planes, and it leads to the formation of bonding and antibonding states [1].

The electronic properties of the bilayer $La_3Ni_2O_7$ are descried by a two-orbital Hubbard model on the bilayer square lattice given as $H_{\text{Hubbard}} = H_t + H_{\text{Int}}$. Here, the kinetic part is given by

$$\begin{aligned} H_t = &\sum_{i\mu\alpha\sigma} \epsilon_\alpha n_{i\mu\alpha\sigma} - \sum_{\langle ij\rangle\mu} t^{\parallel}_{xx}(c^\dagger_{i\mu x\sigma} c_{j\mu x\sigma} + \text{H.c.}) \\ &- \sum_{\langle ij\rangle\mu\sigma} t^{\parallel}_{zx}(c^\dagger_{i\mu z\sigma} c_{j\mu x\sigma} + (z \leftrightarrow x) + \text{H.c.}) \\ &- \sum_{\langle ij\rangle\mu\sigma} t^{\parallel}_{zz}(c^\dagger_{i\mu z\sigma} c_{j\mu z\sigma} + \text{H.c.}) \\ &- \sum_{i\sigma} t^{\perp}_{zz}(c^\dagger_{it z\sigma} c_{ibz\sigma} + \text{H.c.}), \end{aligned} \tag{1}$$

where $c^\dagger_{i\mu\alpha\sigma}$ creates an $\alpha = \{d_{z^2}(z), d_{x^2-y^2}(x)\}$-orbital electron with spin $\sigma = \{\uparrow, \downarrow\}$ at the lattice site i in the layer $\mu = \{\text{top}(t), \text{bottom}(b)\}$; $\langle ij\rangle$ represents the intralayer NN bonds; $t^{\parallel}_{xx}$, $t^{\parallel}_{zx}$, $t^{\parallel}_{zz}$, and $t^{\perp}_{zz}$ are hopping integrals as shown in Fig. 1(a),

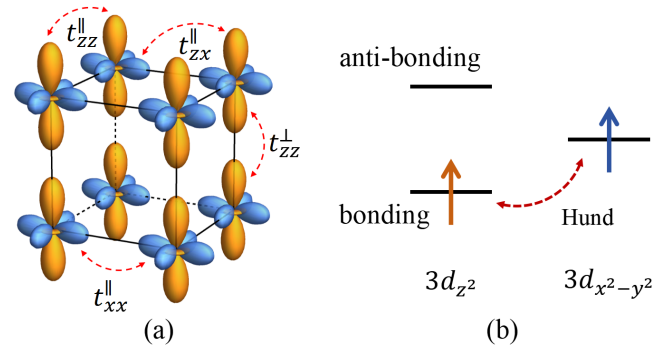

FIG. 1. (a) Schematic illustration of the d_{z^2} and $d_{x^2-y^2}$ orbitals within the bilayer structure of the nickelate $La_3Ni_2O_7$, including the relevant hopping integrals. (b) Strong interlayer hybridization splits the d_{z^2}-band into lower-energy bonding and higher-energy antibonding bands, respectively. The bonding band is energetically favored. Due to strong Hund's coupling, electrons occupying the d_{z^2} and $d_{x^2-y^2}$ orbitals tend to form a spin-triplet state.

of which $t^{\parallel}_{zx}$ represents the nonzero NN hybridization between the two E_g orbitals, exhibiting opposite signs along the x- and y-directions due to the symmetry constraint, $t^{\parallel}_{zx,x} = -t^{\parallel}_{zx,y} = t^{\parallel}_{zx}$; the interlayer hopping of the $d_{x^2-y^2}$ orbital is negligibly small due to its wave-function distribution; and ϵ_α denotes the on-site energy for each orbital.

The interacting part for the two-orbital system is given by

$$\begin{aligned} H_{\text{Int}} = &U \sum_{i\mu\alpha} n_{i\mu\alpha\uparrow} n_{i\mu\alpha\downarrow} + V \sum_{i\mu\sigma\sigma'} n_{i\mu z\sigma} n_{i\mu x\sigma'} \\ &- 2J_H \sum_{i\mu} \left(\boldsymbol{S}_{i\mu z} \cdot \boldsymbol{S}_{i\mu x} + \frac{1}{4} n_{i\mu z} n_{i\mu x} \right) \\ &+ J_H \sum_{i\mu} (c^\dagger_{i\mu z\uparrow} c^\dagger_{i\mu z\downarrow} c_{i\mu x\downarrow} c_{i\mu x\uparrow} + \text{H.c.}). \end{aligned} \tag{2}$$

Here, $\boldsymbol{S}_{i\mu\alpha} = \frac{1}{2} c^\dagger_{i\mu\alpha\sigma} [\boldsymbol{\sigma}]_{\sigma\sigma'} c_{i\mu\alpha\sigma'}$ is the spin operator with Pauli matrices $\boldsymbol{\sigma} = (\sigma_x, \sigma_y, \sigma_z)$, $n_{i\mu\alpha\sigma} = c^\dagger_{i\mu\alpha\sigma} c_{i\mu\alpha\sigma}$ is the particle occupancy number operator, and U and V represent the on-site intra- and interorbital Coulomb repulsions, respectively. Hund's coupling J_H consists of the spin exchange (third term in the second line) and pair-hopping (fourth term in the third line) terms. The pair-hopping term can be omitted when the on-site intraorbital no-double-occupancy condition is imposed. The spin-exchange part favors a spin-triplet formation between the d_{z^2} and $d_{x^2-y^2}$ electrons at the same site, as shown in Fig. 1(b). The condition of orbital rotational symmetry induces $U = V + 2J_H$ [125].

In the strong-coupling limit, the large on-site Hubbard repulsion U prevents the formation of double occupancy for each orbital. When both the d_{z^2} and $d_{x^2-y^2}$ orbitals are singly occupied on the same site, Hund's rule energetically favors the formation of an interorbital spin-triplet ($S = 1$) state. Considering these constraints, the relevant low-energy local Hilbert space at each site comprises eight possible configurations, depicted in Fig. 2.

Treating the kinetic hopping terms as perturbations to the dominant interaction terms, an effective low-energy Hamiltonian can be derived via the superexchange mechanism using

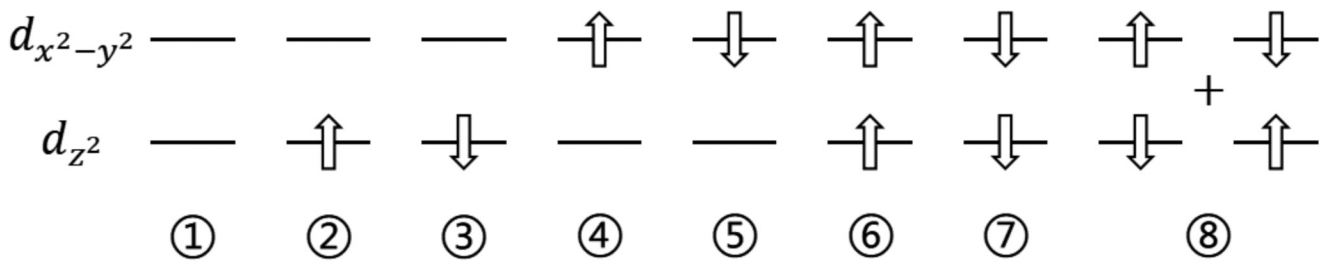

FIG. 2. The low-energy local Hilbert space within a Ni site for the two E_g orbitals (d_{z^2} and $d_{x^2-y^2}$) in the strong-coupling limit upon doping Ni $3d^8$ states, relevant for the derived t-J model. It comprises the double-hole state, spin-$\frac{1}{2}$ singlons, and spin-1 triplet doublons. States with double occupancy within the same orbital are projected out due to strong Coulomb replusion, leaving these eight configurations as the effective basis.

the standard second-order perturbation theory. This procedure yields an effective bilayer t-J-type model that describes the dynamics of the allowed local stats, including spin-$\frac{1}{2}$ singlons (single occupancy in either d_{z^2} or $d_{x^2-y^2}$) and spin-1 triplet doublons (single occupancy in both orbitals). The resulting Hamiltonian is given by

$$H = H_t + H_J^{\parallel} + H_J^{\perp} + V \sum_{i\mu\sigma\sigma'} n_{i\mu z\sigma} n_{i\mu x\sigma'} - 2J_H \sum_{i\mu} \left(\boldsymbol{S}_{i\mu z} \cdot \boldsymbol{S}_{i\mu x} + \frac{1}{4} n_{i\mu z} n_{i\mu x} \right) \tag{3}$$

where H_t represents the effective hopping terms (projected onto the restricted Hilbert space); $H_J^{\parallel}$ and $H_J^{\perp}$ contain the intralayer and interlayer superexchange interactions, respectively. The V- and J_H-terms account for the interorbital Coulomb repulsion and Hund's coupling, respectively, which influence the local energy of each configuration in Fig. 2.

The intralayer superexchange Hamiltonian takes the form

$$\begin{aligned} H_J^{\parallel} = & \sum_{\langle ij\rangle\mu} J_{zz}^{\parallel} \left(\boldsymbol{S}_{i\mu z} \cdot \boldsymbol{S}_{j\mu z} - \frac{1}{4} n_{i\mu z} n_{j\mu z} \right) \\ & + \sum_{\langle ij\rangle\mu} J_{xx}^{\parallel} \left(\boldsymbol{S}_{i\mu x} \cdot \boldsymbol{S}_{j\mu x} - \frac{1}{4} n_{i\mu x} n_{j\mu x} \right) \\ & + \sum_{\langle ij\rangle\mu} J_{dd}^{\parallel} \left(\boldsymbol{S}_{i\mu d} \cdot \boldsymbol{S}_{j\mu d} - \frac{1}{4} n_{i\mu d} n_{j\mu d} \right) \\ & + \sum_{\langle ij\rangle\mu} J_{zx}^{\parallel} \left(\boldsymbol{S}_{i\mu z} \cdot \boldsymbol{S}_{j\mu x} - \frac{1}{4} n_{i\mu z} n_{j\mu x} + (i \leftrightarrow j) \right) \\ & + \sum_{\langle ij\rangle\mu} J_{zd}^{\parallel} \left(\boldsymbol{S}_{i\mu z} \cdot \boldsymbol{S}_{j\mu d} - \frac{1}{4} n_{i\mu z} n_{j\mu d} + (i \leftrightarrow j) \right) \\ & + \sum_{\langle ij\rangle\mu} J_{xd}^{\parallel} \left(\boldsymbol{S}_{i\mu x} \cdot \boldsymbol{S}_{j\mu d} - \frac{1}{4} n_{i\mu x} n_{j\mu d} + (i \leftrightarrow j) \right). \end{aligned} \tag{4}$$

Here, $\boldsymbol{S}_{i\mu\alpha}$ (with $\alpha = z$ or x) represents the spin-$\frac{1}{2}$ operator when there is only one electron occupying the d_{z^2} or $d_{x^2-y^2}$ orbital, respectively. $n_{i\mu\alpha} = \sum_\sigma n_{i\mu\alpha\sigma}$ represents the total particle number of the α orbital at the site i in the layer μ. $\boldsymbol{S}_{i\mu d}$ represents the spin-1 operator under Hund's rule when both the d_{z^2} and $d_{x^2-y^2}$ orbitals are singly occupied, and $n_{i\mu d} = \sum_\alpha n_{i\mu\alpha}$ is the total particle number of the site i in the layer μ under this occupation. The various superexchange parameters J quantify the effective antiferromagnetic spin couplings between different types of local states across NN bonds; for example, $J_{zd}^{\parallel}$ describes the intralayer spin coupling between a d_{z^2} singlon and a triplet doublon. Explicit expressions relating these spin-exchange J parameters to the original Hubbard model parameters are provided in Appendix A. Similarly, we can also derive the interlayer superexchange Hamiltonian:

$$\begin{aligned} H_J^{\perp} = & \sum_i J_{zz}^{\perp} \left(\boldsymbol{S}_{itz} \cdot \boldsymbol{S}_{ibz} - \frac{1}{4} n_{itz} n_{ibz} \right) \\ & + \sum_i J_{dd}^{\perp} \left(\boldsymbol{S}_{itd} \cdot \boldsymbol{S}_{ibd} - \frac{1}{4} n_{itd} n_{ibd} \right) \\ & + \sum_i J_{zx}^{\perp} \left(\boldsymbol{S}_{itz} \cdot \boldsymbol{S}_{ibx} - \frac{1}{4} n_{itz} n_{ibx} + (t \leftrightarrow b) \right) \\ & + \sum_i J_{zd}^{\perp} \left(\boldsymbol{S}_{itz} \cdot \boldsymbol{S}_{ibd} - \frac{1}{4} n_{itz} n_{ibd} + (t \leftrightarrow b) \right) \\ & + \sum_i J_{xd}^{\perp} \left(\boldsymbol{S}_{itx} \cdot \boldsymbol{S}_{ibd} - \frac{1}{4} n_{itx} n_{ibd} + (t \leftrightarrow b) \right). \end{aligned} \tag{5}$$

Various interlayer superexchange parameters J are defined in a similar way to those of the intralayer ones, and their expressions are also derived in Appendix A. The interlayer superexchange within a rung for the singly occupied $d_{x^2-y^2}$-orbital spin-$\frac{1}{2}$ approximate to 0 due to the negligible interlayer hopping between them. To demonstrate the validity of the perturbation theory, we also solve the two-orbital Hubbard model combining Eqs. (1) and (2) on small-sized lattices of small sizes using exact diagonalization (ED) and DMRG methods. The results are provided in Appendix C.

We adopt the data obtained from the DFT calculations [42] as input physical parameters for H_t. The intralayer hopping parameters are $t_{zz}^{\parallel} = 0.110\,\text{eV}$, $t_{zx}^{\parallel} = 0.239\,\text{eV}$, and $t_{xx}^{\parallel} = 0.483\,\text{eV}$. The interlayer hopping for the d_{z^2} orbital is $t_{zz}^{\perp} = 0.635\,\text{eV}$, while the ones involving the $d_{x^2-y^2}$ orbital nearly vanish. The on-site energies are set to $\epsilon_z = 0.409\,\text{eV}$ and $\epsilon_x = 0.776\,\text{eV}$. With the relationship of interaction strengths $U = V + 2J_H$ [125], the on-site Coulomb repulsion is chosen as $U = 5\,\text{eV}$, and Hund's coupling J_H ranges from $\frac{U}{8}$ to $\frac{U}{4}$ approximately.

III. SLAVE-PARTICLE MEAN-FIELD STUDY

In this section, we present the construction of the physical Hilbert space and apply the slave-particle mean-field theory to study the superconducting state.

A. Constructions of physical states

Within the framework of the slave-particle method, the restriction to the physical Hilbert space can be systematically imposed. The fully empty $3d^6$ state is defined by acting with the holon creation operator $h^\dagger_{i\mu}$ on a fictitious vacuum state,

$$|\text{empty}\rangle_{i\mu} = h^\dagger_{i\mu}|\text{vac}\rangle_{i\mu}, \tag{6}$$

where $|\text{vac}\rangle$ represents the vacuum of slave particles and lies outside the physical space. For simplicity, the on-site energy of the empty state $|\text{empty}\rangle_{i\mu}$ in the atomic limit is set to zero, and its occupancy number is denoted by $\tilde{n}_h$.

The four singly occupied $3d^7$ states, corresponding to the spin-$\frac{1}{2}$ singlon configurations shown in Fig. 2, are represented using bosonic spinon creation operators,

$$\begin{aligned} |\uparrow_z\rangle_{i\mu} &= b^\dagger_{i\mu z\uparrow}|\text{vac}\rangle_{i\mu}, \quad |\uparrow_x\rangle_{i\mu} = b^\dagger_{i\mu x\uparrow}|\text{vac}\rangle_{i\mu}, \\ |\downarrow_z\rangle_{i\mu} &= b^\dagger_{i\mu z\downarrow}|\text{vac}\rangle_{i\mu}, \quad |\downarrow_x\rangle_{i\mu} = b^\dagger_{i\mu x\downarrow}|\text{vac}\rangle_{i\mu}, \end{aligned} \tag{7}$$

where $b^\dagger_{i\mu\alpha\sigma}$ is a creation operator of bosonic spinon, acting on the vacuum state to generate four spin-$\frac{1}{2}$ configurations. The occupancy numbers for these singly occupied state are $\tilde{n}_x$ and $\tilde{n}_z$ for the $3d_{x^2-y^2}$ and $3d_{z^2}$ orbitals, respectively. The corresponding spin-$\frac{1}{2}$ operators are defined in the conventional manner. For instance, the spin operator for a state with only the $d_{x^2-y^2}$ orbital occupied is given by $\boldsymbol{S}_{i\mu x} = \frac{1}{2}b^\dagger_{i\mu x\sigma}[\boldsymbol{\sigma}]_{\sigma\sigma'}b_{i\mu x\sigma'}$, where $\boldsymbol{\sigma} = (\sigma_x, \sigma_y, \sigma_z)$ are the Pauli matrices. The on-site energy of the singly occupied state in the d_{z^2} orbital is set to zero, while for the $d_{x^2-y^2}$ orbital, a finite energy difference $\Delta_g = \epsilon_x - \epsilon_z$ is considered.

For the three $3d^8$ spin-1 triplet doublons, we employ a three-component Schwinger fermion representation. The Schwinger fermion $f_{i\mu} = (f_{i\mu,+1}, f_{i\mu,0}, f_{i\mu,-1})^T$ labels each spin projection:

$$\begin{aligned} |+1\rangle_{i\mu} &= f^\dagger_{i\mu,+1}|\text{vac}\rangle_{i\mu}, \\ |0\rangle_{i\mu} &= f^\dagger_{i\mu,0}|\text{vac}\rangle_{i\mu}, \\ |-1\rangle_{i\mu} &= f^\dagger_{i\mu,-1}|\text{vac}\rangle_{i\mu}. \end{aligned} \tag{8}$$

The corresponding spin-1 operators are expressed as

$$\begin{aligned} \hat{S}^+_{i\mu d} &= f^\dagger_{i\mu}S_+f_{i\mu} = \sqrt{2}(f^\dagger_{i\mu,+1}f_{i\mu,0} + f^\dagger_{i\mu,0}f_{i\mu,-1}), \\ \hat{S}^-_{i\mu d} &= f^\dagger_{i\mu}S_-f_{i\mu} = \sqrt{2}(f^\dagger_{i\mu,0}f_{i\mu,+1} + f^\dagger_{i\mu,-1}f_{i\mu,0}), \\ \hat{S}^z_{i\mu d} &= f^\dagger_{i\mu}S_zf_{i\mu} = f^\dagger_{i\mu,+1}f_{i\mu,+1} - f^\dagger_{i\mu,-1}f_{i\mu,-1}, \end{aligned} \tag{9}$$

where the ladder operators are $\hat{S}^\pm_{i\mu} = \hat{S}^x_{i\mu} \pm i\hat{S}^y_{i\mu}$, and the matrices $\{S_+, S_-, S_z\}$ form the spin-1 irreducible representation of the SU(2) generators. The occupancy number of these spin-triplet states is denoted as $\tilde{n}_d$. The on-site energy of these spin-1 states is set to $V - J_H + \Delta_g$.

The original electron operators can be expressed in terms of these slave particle operators. For example, the creation operator for a $d_{x^2-y^2}$-orbital electron at site i in layer μ with spin $\uparrow$ is

$$c^\dagger_{i\mu x\uparrow} = f^\dagger_{i\mu,+1}b_{i\mu z\uparrow} + \frac{1}{\sqrt{2}}f^\dagger_{i\mu,0}b_{i\mu z\downarrow} + b^\dagger_{i\mu x\uparrow}h_{i\mu}, \tag{10}$$

with similar expressions for the spin-$\downarrow$ state and the d_{z^2} orbital. To preserve fermionic statistics, we assign fermionic statistics to both f- and h-operators, while the b-operators are bosonic. The physical Hilbert space is further constrained by the following local condition:

$$\begin{aligned} &f^\dagger_{i\mu,+1}f_{i\mu,+1} + f^\dagger_{i\mu,0}f_{i\mu,0} + f^\dagger_{i\mu,-1}f_{i\mu,-1} \\ &\quad + h^\dagger_{i\mu}h_{i\mu} + b^\dagger_{i\mu x\uparrow}b_{i\mu x\uparrow} + b^\dagger_{i\mu x\downarrow}b_{i\mu x\downarrow} \\ &\quad + b^\dagger_{i\mu z\uparrow}b_{i\mu z\uparrow} + b^\dagger_{i\mu z\downarrow}b_{i\mu z\downarrow} = 1, \end{aligned} \tag{11}$$

which corresponds to a local U(1) gauge symmetry associated with charge conservation. For an averaged $3d^{7.5}$ configuration relevant to $La_3Ni_2O_7$, the occupancy numbers are further related by $\tilde{n}_d - \tilde{n}_h = 0.5$.

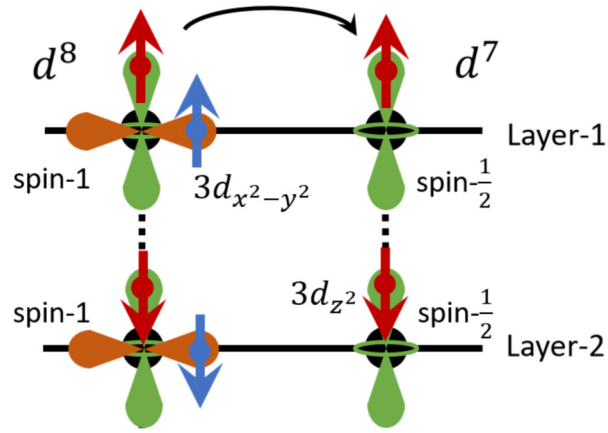

FIG. 3. Schematic illustration of the two types of interlayer singlet bonds formed on a rung (vertical pair of sites) driven by strong interlayer superexchange. Left: A spin-1 singlet bond formed between two local spin-triplets (characteristic of the d^8 electronic configuration). Right: A spin-1 singlet bond formed between two localized spins (predominantly d_{z^2} electrons, characteristic of the d^7 configuration emerging upon doping).

B. Correlated pairing—Mixed spin-1 and spin-$\frac{1}{2}$ valence bonds

When interlayer superexchange dominates, the two localized spin-triplet states along a rung tend to form a spin-1 singlet bond, as illustrated in Fig. 3. The corresponding rung spin-singlet pairing operator at lattice site j is given by

$$F^\dagger_j = \frac{1}{\sqrt{3}}(f^\dagger_{jt,1}f^\dagger_{jb,-1} - f^\dagger_{jt,0}f^\dagger_{jb,0} + f^\dagger_{jt,-1}f^\dagger_{jb,1}). \tag{12}$$

This describes the formation of a spin-1 singlet bond between neighboring sites jt and jb on a rung. In the mother $3d^8$ configuration, the system forms a spin-1 interlayer valence-bond solid (VBS) state, where the four electrons residing in the two E_g orbitals are strongly entangled, forming an interlayer spin singlet on each rung.

In the case of $La_3Ni_2O_7$, however, the actual electronic configuration is closer to $3d^{7.5}$, where additional holes

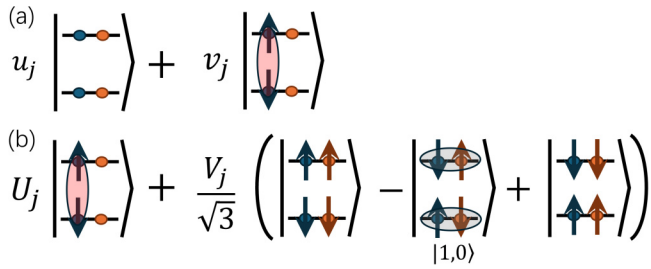

FIG. 4. Schematic diagrams for the conventional BCS pairing (a) and the correlated pairing given by Eq. (14) (b). The former is represented as a coherent superposition of a fully paired electron state and the vacuum state. The latter is a superposition of two valence bond singlets composed by a pair of spin-1 and a pair of spin-$\frac{1}{2}$ states, respectively. The blue circles represent the d_{z^2} orbitals, while the orange ones represent the $d_{x^2-y^2}$ orbitals. $|1,0\rangle$ means a triplet with total spin $S=1$ and total z-component spin S^z.

prefer to occupy the $d_{x^2-y^2}$ orbitals. This emergence of SC in $La_3Ni_2O_7$ under pressure can be considered as doping the d^8 spin-1 VBS state. Upon doping, the spin-triplet configuration, characteristic of the $3d^8$ VBS, largely reduces to a $3d^7$ spin-$\frac{1}{2}$ configuration, predominantly involving the d_{z^2} orbital electron. As a result, the occupancy number of the spin-1 states, denoted n_1, is approximately 0.5, and the occupancy number of the spin-$\frac{1}{2}$ states in the d_{z^2} orbital, n_z, is similarly around 0.5. Consequently, the strong interlayer exchange $J_{zz}^{\perp}$ drives the formation of a spin-$\frac{1}{2}$ singlet bond along the rungs:

$$B_j^\dagger = \frac{1}{\sqrt{2}}(b_{jtz\uparrow}^\dagger b_{jbz\downarrow}^\dagger - b_{jtz\downarrow}^\dagger b_{jbz\uparrow}^\dagger), \tag{13}$$

where the $d_{x^2-y^2}$ orbital remains essentially empty on the rungs. This description captures the fundamental change in the electronic structure as the system transitions from a spin-1 to a spin-$\frac{1}{2}$-dominated regime.

The nature of superconducting pairing in this doped spin-1 VBS state is fundamentally different from that of Cooper pairs in a Bardeen-Cooper-Schrieffer (BCS) superconductor [126], as depicted in Fig. 4. In a conventional superconductor, the BCS wave function is a coherent superposition of the fully paired electron state and the vacuum (empty) state. In contrast, the exotic spinon pairing mechanism considered here involves a combination of two distinct singlets: one associated with spin-$\frac{1}{2}$ singlet states and the other with spin-1 singlet states. In the slave-particle formalism, this pairing can be represented as

$$|\text{spinon pair}\rangle = \prod_j (U_j B_j^\dagger + V_j F_j^\dagger)|\text{vac}\rangle, \tag{14}$$

where U_j, V_j are coefficients that reflect the relative weights of the two components. This mixed pairing structure reflects the complex interplay between spin-1 and spin-$\frac{1}{2}$ physics in the doped system, and the resulting physical electron pairing emerges as a composite of these slave-particle pairings.

C. Slave-particle mean-field results

Based on the preceding model analysis, we perform a slave-particle mean-field calculation using the Hamiltonian Eq. (3) on the $2\times200\times200$ bilayer lattice with the temperature 10^{-4} to further investigate the physical picture described earlier. In this mean-field approach, we concentrate on the SC pairing channels. The superexchange terms considered most relevant and consequently decoupled into spin-singlet pairing channels are as follows: the interlayer spin-1 interaction $J_{dd}^{\perp}\boldsymbol{S}_{itd}\cdot\boldsymbol{S}_{ibd}$, the interlayer $3d_{z^2}$ spin-$\frac{1}{2}$ interaction $J_{zz}^{\perp}\boldsymbol{S}_{itz}\cdot\boldsymbol{S}_{ibz}$, and the intralayer $3d_{x^2-y^2}$ spin-$\frac{1}{2}$ interaction $J_{xx}^{\parallel}\boldsymbol{S}_{i\mu x}\cdot\boldsymbol{S}_{j\mu x}$. The decoupling of the spin-$\frac{1}{2}$ exchange interactions follows the conventional slave-boson mean-field theory [122]. For the spin-1 interactions, the pairing and hopping order parameters for the total spin-singlet channels are introduced as

$$\Delta_0^\dagger = \frac{1}{\sqrt{3}}(f_{it,+1}^\dagger f_{id,-1}^\dagger - f_{it,0}^\dagger f_{id,0}^\dagger + f_{it,-1}^\dagger f_{id,+1}^\dagger),$$
$$\chi_0^\dagger = \frac{1}{\sqrt{3}}(f_{it,+1}^\dagger f_{id,+1} + f_{it,0}^\dagger f_{id,0} + f_{it,-1}^\dagger f_{id,-1}).$$

Here, $\Delta_0^\dagger$ corresponds to the rung spin-singlet pairing operator $F_i^\dagger$. The spin-1 exchange interaction can then be decoupled into these singlet channels as

$$\boldsymbol{S}_{it}\cdot\boldsymbol{S}_{id} = -2\Delta_0^\dagger\Delta_0 - 2\chi_0^\dagger\chi_0. \tag{15}$$

In this mean-field decoupling scheme, contributions from higher-energy nonsinglet channels (e.g., total spin-1 and spin-2 configurations) are omitted. The resulting mean-field hopping and pairing order parameters are then determined by solving the equations self-consistently. See Appendix B for the details.

Several other terms present in the full Hamiltonian Eqs. (4) and (5) are neglected within this mean-field ansatz. Terms coupling the spin-1 doublon state (f-fermion) with spin-$\frac{1}{2}$ singlon states (b-boson), such as $\boldsymbol{S}_d\cdot\boldsymbol{S}_x$ and $\boldsymbol{S}_d\cdot\boldsymbol{S}_z$, do not lead to pairing and are therefore omitted. Additionally, other superexchange terms like the intralayer $\boldsymbol{S}_z\cdot\boldsymbol{S}_z$ and $\boldsymbol{S}_z\cdot\boldsymbol{S}_x$, as well as the interlayer $\boldsymbol{S}_x\cdot\boldsymbol{S}_x$ and $\boldsymbol{S}_z\cdot\boldsymbol{S}_x$, are assumed to have significantly weaker coupling strengths and thus negligible contributions to the primary pairing mechanism; these are also omitted for simplicity. These approximations allow us to focus more clearly on the behavior of the on-site occupancy numbers and dominant pairing amplitudes as functions of Hund's coupling J_H and doping levels. Importantly, our mean-field approach does not decouple the on-site interorbital Coulomb repulsion V or the Hund's coupling J_H terms. A naive mean-field decomposition of Hund's coupling, for instance, could generate unphysical intraion triplet pairing. These crucial on-site terms (V and J_H) are instead treated exactly by modifying the local on-site energies of the physical slave-particle states, as detailed in the previous sections.

The calculated on-site occupancy numbers as a function of J_H are shown in Fig. 5(a). Here, $\tilde{n}_d$ represents the on-site occupancy number for spin-1 state, while $\tilde{n}_z$ and $\tilde{n}_x$ correspond to the on-site occupancy numbers for the spin-$\frac{1}{2}$ states in the d_{z^2} and $d_{x^2-y^2}$ orbitals, respectively. Additionally, $\tilde{n}_h$ denotes the occupancy of the empty state.

Figure 5(a) reveals the physical figure that Hund's coupling J_H promotes the combination of a d_{z^2} singlon and a $d_{x^2-y^2}$ singlon into a spin-1 triplet doublon and a double-hole state, while the hybridization induces the transformation of the d_{z^2}

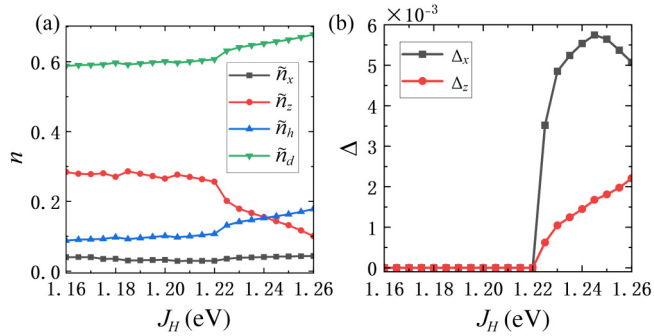

FIG. 5. Results based on the SPMF method results as a function of Hund's coupling J_H. Plotted are (a) the on-site occupancy numbers $(\tilde{n}_x, \tilde{n}_z, \tilde{n}_h, \tilde{n}_d)$ of different local electronic configurations, and (b) the interlayer singlet pairing amplitudes (Δ_x, Δ_z). The results indicate that superconducting pairing is triggered by increasing J_H, and the contribution is dominated by the interlayer pairing Δ_x of the $d_{x^2-y^2}$ orbital.

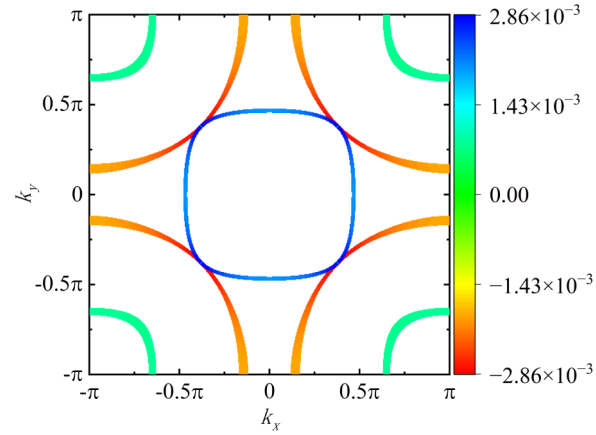

FIG. 6. The projected superconducting gap distribution on the Fermi surface from the SPMF calculations.

singlons into the $d_{x^2-y^2}$ singlons, resulting in the decreased $\tilde{n}_z$, increased $\tilde{n}_h$ and $\tilde{n}_d$, and the almost unchanged $\tilde{n}_x$. This result is consistent with our analysis of low-energy subspace, which points out that the transformation of two spin-$\frac{1}{2}$ singlons into a spin-1 doublon and a double-hole state lifts the energy of $V - J_H$ (see Appendix A for more details), a process that will be more likely to occur when J_H increases. Furthermore, the noise behavior appearing in Fig. 5(a) results from the finite-size effect, which does not affect the critical physical figure captured.

In the atomic limit, there is one electron in the d_{z^2} orbital, and a half electron in the $d_{x^2-y^2}$ orbital. In the slave-particle picture outlined in Fig. 2, the occupation numbers for the spin-1 state and the spin-$\frac{1}{2}$ state in the d_{z^2} orbital are both 0.5. Then

$$\tilde{n}_d = \tilde{n}_z = 0.5, \quad \tilde{n}_x = \tilde{n}_h = 0. \tag{16}$$

However, the presence of intraorbital hopping and interorbital hybridization leads to significant deviations from these idealized atomic orbital occupancies. A key factor influencing these deviations is Hund's coupling, J_H. As J_H increases, the on-site energy of the doublon states is systematically lowered, rendering these configuration energetically more favorable Consequently, there is an enhanced tendency for spinons originating from the $3d_{x^2}$ and $3d_{z^2-y^2}$ orbitals to combine and form doublon-holon pairs. This process manifests as an increase in the calculated average doublon $(\tilde{n}_d)$ and $(\tilde{n}_h)$ occupancies. It is noteworthy that while both $\tilde{n}_d$ and $\tilde{n}_h$ increase, their difference $(\tilde{n}_d - \tilde{n}_h$, related to the net doping) remains constant.

Simultaneously, the occupancy $\tilde{n}_z$ of singly occupied $3d_{z^2}$ orbitals decreases, whereas the $3d_{x^2-y^2}$ orbital occupancy $\tilde{n}_x$ shows minimal variation. These observations indicate a shift in the balance between the spin-1 and spin-$\frac{1}{2}$ states as Hund's coupling strengthens. The sensitivity of the on-site occupancy numbers to J_H reflects the delicate balance between intraorbital and interorbital interactions in determining the electronic ground state.

In real materials, SC is ultimately characterized by physical electron Cooper pairs. The interlayer spin-1 singlet pairing introduced above constitutes both interlayer spin-$\frac{1}{2}$ singlet and triplet pairings for the $3d_{x^2-y^2}$ and $3d_{z^2}$ orbitals, while the singlet pairing channels are dominated. The physical interlayer singlet pairing amplitudes for electrons in the $3d_{x^2-y^2}$ and $3d_{z^2}$ orbitals, Δ_x and Δ_z, can be understood as arising from the projection of the fundamental slave-particle pairing Δ_0 onto these specific orbital channels. Crucially, the establishment of phase coherence for these physical electron pairs depends on the condensation of bosonic singlons. Consequently, the effective pairing amplitudes can be schematically expressed as $\Delta_x \sim \tilde{n}_z\langle\Delta_0\rangle$ and $\Delta_z \sim \tilde{n}_x\langle\Delta_0\rangle$.

An intriguing outcome of this formalism is that the phase coherence of the $3d_{x^2-y^2}$ interlayer pairing Δ_x is thus intrinsically linked to, and effectively controlled by, the occupancy and coherence of $3d_{z^2}$ singlons (and *vice versa* for Δ_z). This relationship is consistent with the underlying slave-particle construction: a local spin-1 doublon consists of one electron in the $3d_{x^2-y^2}$ orbital and one in the $3d_{z^2}$ orbital. If a hole is introduced into the $3d_{x^2-y^2}$ component of this doublon, i.e., if the $d_{x^2-y^2}$ electron is removed, the remnant on that site is a $3d_{z^2}$ singlon. The dynamics of these singlons are therefore essential for the emergence of the physical superconducting state.

Figure 5(b) shows the J_H dependence of the pairing amplitude for interlayer singlet pairing in the d_{z^2} and $d_{x^2-y^2}$ orbitals. As expected, pairing emerges rapidly with increasing J_H, with the interlayer pairing amplitude Δ_x dominating across the entire parameter range. This dominance of interlayer pairing originates from the robust interlayer spin-1 superexchange, which drives the formation of the rung pairs in this bilayer structure. Meanwhile, the d_{z^2} pairing is suppressed by the small $d_{x^2-y^2}$ singlon number, leading to the dominance of the $d_{x^2-y^2}$ pairing. As the main contributor to the superconducting pairing is the spin-1 doublon, when J_H increases within a certain range, the increasing $\tilde{n}_d$ enhances $\langle\Delta_0\rangle$ promptly, and thus enhances Δ_z and Δ_x promptly.

To further analyze the superconducting pairing symmetry, we calculate the projected superconducting gap distribution on the Fermi surface in Fig. 6. The results indicates that the local interlayer pairing results in an extended s-wave order parameter with a fully gapped Fermi surface.

In addition, the effect of doping on the electronic structure and pairing behavior is investigated, as illustrated in Fig. 7.

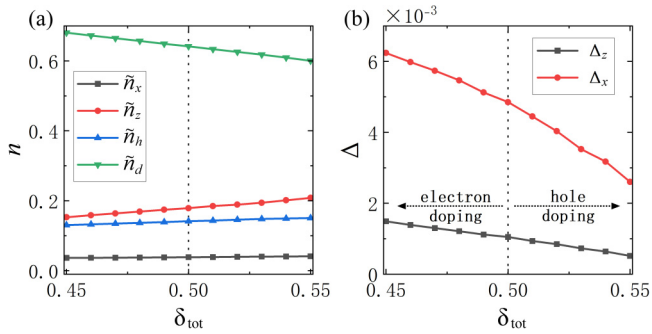

FIG. 7. SPMF results as functions of the total hole density $\delta_{\rm tot}$ (where $\delta_{\rm tot} = 0.5$ corresponds to the nominal $d^{7.5}$ configuration in $La_3Ni_2O_7$). (a) On-site occupancy numbers for the different local states. (b) Interlayer singlet pairing amplitudes. A clear trend is observed where electron doping ($\delta_{\rm tot} < 0.5$, increased electron density) enhances the superconducting pairing amplitude (primarily the dominant Δ_x), while hole doping ($\delta_{\rm tot} > 0.5$) has the opposite effect.

The total hole density $\delta_{\rm tot} = 0.5$ corresponds to the nominal $3d^{7.5}$ electronic configuration of Ni in the $La_3Ni_2O_7$. Hole doping ($\delta_{\rm tot} > 0.5$) and electron doping (<0.5) alter the occupancy numbers in distinct ways. As shown in Fig. 7(a), hole doping tends to reduce $\tilde{n}_d$ while increasing both $\tilde{n}_x$ and $\tilde{n}_z$. Conversely, electron doping increases $\tilde{n}_d$ while decreasing $\tilde{n}_x$ and $\tilde{n}_z$. Also, the difference between the doublon and holon is fixed, $\tilde{n}_d - \tilde{n}_h = \delta_{\rm tot}$.

The superconducting pairing amplitude, shown in Fig. 7(b), exhibits a clear dependence on doping, with the interlayer $d_{x^2-y^2}$ pairing amplitude Δ_x remaining dominant across the full doping range. As hole doping increases, the pairing amplitudes decrease, suggesting that hole doping weakens the overall superconducting state. In contrast, electron doping enhances the pairing amplitudes.

IV. DENSITY MATRIX RENORMALIZATION-GROUP STUDY

To further corroborate the physical picture derived above, we employ the state-of-the-art DMRG method [123,124] at zero temperature.

The DMRG calculations are performed using tensor libraries TensorKit [127] and FiniteMPS [128], which provide an implementation of the required $U(1)_{\rm charge} \times SU(2)_{\rm spin}$ symmetries [129,130]. Since the bond dimension D is constrained by computational complexity, the DMRG simulation struggles to accurately solve two-dimensional (2D) systems. In our work, we investigate the model on one-dimensional (1D) geometries of sizes $2 \times 1 \times 96$ and $2 \times 2 \times 48$ with open boundary conditions in all directions. Although this setup deviates significantly from genuine bilayer 2D systems, we can still predict the existence and strength of order parameters in 2D systems by analyzing the decay behavior of the corresponding correlation functions in the 1D systems. The matrix product state (MPS) representation is constructed using a zigzag path along the ladder, as illustrated in Fig. 8. We retain up to $D = 10\,000$ $U(1)_{\rm charge} \times SU(2)_{\rm spin}$ multiplets in the DMRG simulations and a convergence threshold of 10^{-8} for the ground-state energy.

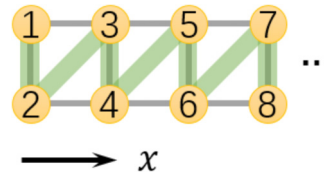

FIG. 8. Illustration of the zigzag path used in the DMRG calculations for the $2 \times 1 \times L_x$ ladder.

To characterize the ground-state properties, we numerically simulate the particle-number distribution and various correlation functions. The particle-number operator for orbital α at site i (averaged over the two layers) is defined as

$$n_{i\alpha} = \frac{1}{2}\sum_{\mu\sigma} c^\dagger_{i\mu\alpha\sigma} c_{i\mu\alpha\sigma}, \tag{17}$$

where $c^\dagger_{i\mu\alpha\sigma}$ creates an electron in orbital α with spin-σ at lattice site i in layer μ. Its expectation value yields the particle-number distribution. The single-particle correlation function for the combination of d_{z^2} and $d_{x^2-y^2}$ orbitals is given by

$$G(r) = \frac{1}{4}\sum_{\mu\sigma}\langle (c^\dagger_{i\mu z\sigma} + c^\dagger_{i\mu x\sigma})(c_{j\mu z\sigma} + c_{j\mu x\sigma}) + \text{H.c.}\rangle, \tag{18}$$

where $r = |i - j|$ is the distance between the sites i and j. The charge-density correlation function for the α-orbital is defined as

$$D_\alpha(r) = \langle n_{i\alpha} n_{j\alpha}\rangle - \langle n_{i\alpha}\rangle\langle n_{j\alpha}\rangle. \tag{19}$$

The spin-spin correlation function averaged over layers is given by

$$F(r) = \frac{1}{2}\sum_{\mu}\langle \boldsymbol{S}_{i\mu}\cdot\boldsymbol{S}_{j\mu}\rangle, \tag{20}$$

where $\boldsymbol{S}_{i\mu} = \boldsymbol{S}_{i\mu z} + \boldsymbol{S}_{i\mu x} + \boldsymbol{S}_{i\mu d}$ is the total spin operator at site i in layer μ, containing contributions from d_{z^2} singlons, $d_{x^2-y^2}$ singlons, and doublon states.

To characterize the superconducting tendencies, we investigate various pairing channels. The interlayer ($\perp$) and intralayer ($\parallel$) pairing operators are given by

$$\Delta^{\perp\dagger}_{i\alpha} = \frac{1}{\sqrt{2}}(c^\dagger_{it\alpha\uparrow}c^\dagger_{ib\alpha\downarrow} - c^\dagger_{it\alpha\downarrow}c^\dagger_{ib\alpha\uparrow}),$$
$$\Delta^{\parallel\dagger}_{i\mu\alpha} = \frac{1}{\sqrt{2}}(c^\dagger_{i\mu\alpha\uparrow}c^\dagger_{i+1,\mu\alpha\downarrow} - c^\dagger_{i\mu\alpha\downarrow}c^\dagger_{i+1,\mu\alpha\uparrow}). \tag{21}$$

The long-distance behavior of these pairings is characterized by their correlation functions:

$$\Phi^\perp_\alpha(r) = \langle \Delta^{\perp\dagger}_{i\alpha}\Delta^\perp_{j\alpha}\rangle,$$
$$\Phi^\parallel_\alpha(r) = \frac{1}{2}\sum_\mu\langle \Delta^{\parallel\dagger}_{i\mu\alpha}\Delta^\parallel_{j\mu\alpha}\rangle. \tag{22}$$

In a 1D system, pairing correlations in each channel typically decay algebraically as $r^{-K_{\rm SC}}$, leading to quasi-long-ranged order. Here, the decay power exponent $K_{\rm SC}$ is related to the Luttinger parameter of the corresponding channel, and a value $K_{\rm SC} < 2$ generally indicates a divergence of superconductivity

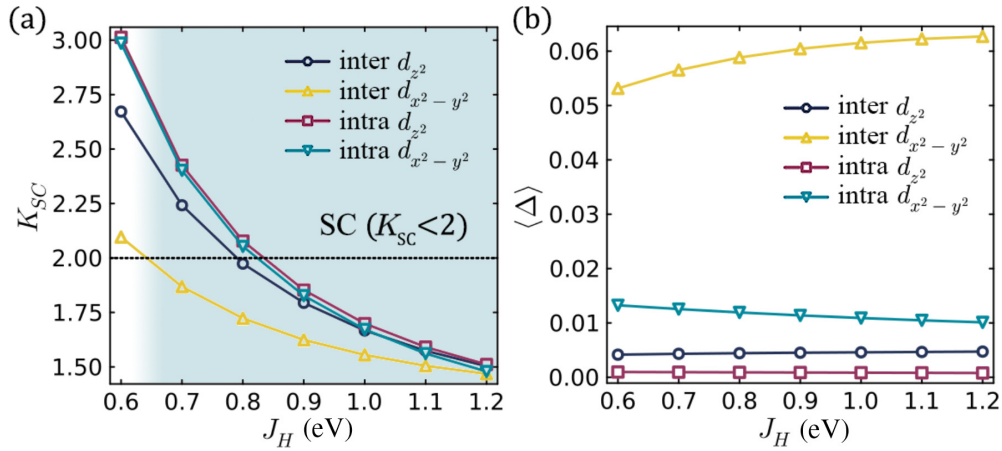

FIG. 9. DMRG results as functions of Hund's coupling J_H. (a) The decay power $K_{\rm SC}$ of singlet pairing correlations $\Phi_\alpha^\perp(r)$ and $\Phi_\alpha^\parallel(r)$ in the d_{z^2} and $d_{x^2-y^2}$ orbitals, respectively. The legends *inter* and *intra* correspond to $\Phi_\alpha^\perp(r)$ and $\Phi_\alpha^\parallel(r)$, respectively. Superconductivity ($K_{\rm SC}<2$) is indicated for $J_H>0.7$ eV, dominated by interlayer $d_{x^2-y^2}$ pairing with the lowest $K_{\rm SC}$. (b) The singlet pairing order parameters $\langle\Delta_\alpha^\perp\rangle$ and $\langle\Delta_\alpha^\parallel\rangle$.

susceptibility in each channel. The channel with the smallest value of $K_{\rm SC}$ is the dominant one. Furthermore, due to the limitations of the $\mathrm{U(1)_{charge}}\times\mathrm{SU(2)_{spin}}$ symmetry, we define the square root of the structure factors as the singlet pairing order parameters,

$$\langle\Delta_\alpha^\perp\rangle=\sqrt{\frac{1}{N_b}\sum_{i,j}\langle\Delta_{i\alpha}^{\perp\dagger}\Delta_{j\alpha}^{\perp}\rangle},$$
$$\langle\Delta_\alpha^\parallel\rangle=\sqrt{\frac{1}{2N_b}\sum_{i,j,\mu}\langle\Delta_{i\mu\alpha}^{\parallel\dagger}\Delta_{j\mu\alpha}^{\parallel}\rangle},\tag{23}$$

where the sums over i, j are restricted to $\frac{L_x}{4}\leqslant i,j\leqslant\frac{3L_x}{4}$, and N_b is the number of contributing pairs in the sum.

Similarly, the triplet pairing operators (denoted by superscript t) are formulated as

$$\begin{aligned}\Delta_{i\alpha}^{t,\perp\dagger}&=c_{it\alpha\uparrow}^\dagger c_{ib\alpha\uparrow}^\dagger+c_{it\alpha\downarrow}^\dagger c_{ib\alpha\downarrow}^\dagger\\&\quad+\frac{1}{\sqrt{2}}(c_{it\alpha\uparrow}^\dagger c_{ib\alpha\downarrow}^\dagger+c_{it\alpha\downarrow}^\dagger c_{ib\alpha\uparrow}^\dagger),\\\Delta_{i\mu\alpha}^{t,\parallel\dagger}&=c_{i\mu\alpha\uparrow}^\dagger c_{i+1,\mu\alpha\uparrow}^\dagger+c_{i\mu\alpha\downarrow}^\dagger c_{i+1,\mu\alpha\downarrow}^\dagger\\&\quad+\frac{1}{\sqrt{2}}(c_{i\mu\alpha\uparrow}^\dagger c_{i+1,\mu\alpha\downarrow}^\dagger+c_{i\mu\alpha\downarrow}^\dagger c_{i+1,\mu\alpha\uparrow}^\dagger).\end{aligned}\tag{24}$$

The corresponding triplet pairing correlation functions are

$$\Phi_\alpha^{t,\perp}(r)=\langle\Delta_{i\alpha}^{t,\perp\dagger}\Delta_{j\alpha}^{t,\perp}\rangle,$$
$$\Phi_\alpha^{t,\parallel}(r)=\frac{1}{2}\sum_\mu\langle\Delta_{i\mu\alpha}^{t,\parallel\dagger}\Delta_{j\mu\alpha}^{t,\parallel}\rangle.\tag{25}$$

The impact of Hund's coupling on SC and particle distribution, as determined by the DMRG calculations, is presented in Fig. 9. In Fig. 9(a), the emergence of the superconducting ($K_{\rm SC}<2$) corresponds to the region where $J_H\gtrsim0.7$ eV. Across the investigated range of J_H from 0.6 to 1.2 eV, interlayer singlet pairing in the $d_{x^2-y^2}$ orbital is consistently dominant, and the strength of this superconducting tendency increases monotonically with J_H. For $J_H\gtrsim1$, the differences in $K_{\rm SC}$ values among the various strong pairing channels become less significant, potentially due to proximity effects between competing or coexisting orders. To further substantiate the dominance of the interlayer $d_{x^2-y^2}$ orbital pairing, the pairing order parameters $\langle\Delta_\alpha^\perp\rangle$ and $\langle\Delta_\alpha^\parallel\rangle$ are also calculated, as shown in Fig. 9(b).

Focusing on the representative case of $J_H=1$eV, additional detailed ground-state properties are presented in Figs. 10 and 11. Figure 10(a) displays the particle number distribution in the two E_g orbitals. The interlayer and intralayer singlet pairing correlation functions, shown in Figs. 10(b) and 10(c), respectively, both exhibit clear algebraic decay. This behavior is characteristic of a Luther-Emery liquid, where spin excitations are gapped, allowing for dominant superconducting correlations [131]; also see below for the behavior of spin excitation. Furthermore, the charge density correlation function, depicted in Fig. 10(d), also decays algebraically. This latter finding suggests that the full two-dimensional system might exhibit a complex interplay or coexistence of SC and charge density wave ordering, with the interlayer $d_{x^2-y^2}$ orbital as the primary source of SC.

In addition, a typical 1D single-orbital Luther-Emery liquid has the property $K_{\rm SC}\times K_\rho=1$, while our simulation results show that $K_{\rm SC}^\alpha\times K_\rho^\alpha$ range from 2.3 to 2.6. The deviation results from the combination of the strong interorbital interactions and the geometrical structure of the ladder, which allows the $2\times1\times L_x$ two-orbital system to be physically mapped to a four-orbital system with complex interorbital interactions, deviating from a strict 1D single-orbital system.

As shown in Fig. 11(a), the single-particle correlation function $G(r)$ exhibits exponential decay, indicating the gapped charge degree of freedom. The spin-spin correlation function $F(r)$, presented in Fig. 11(b), also exhibits exponential decay, confirming the presence of a spin gap, consistent with the Luther-Emery liquid picture. Of course, the spin gap is a result of the ladder, and the existence of magnetic order in the bulk bilayer square lattice remains an open question.

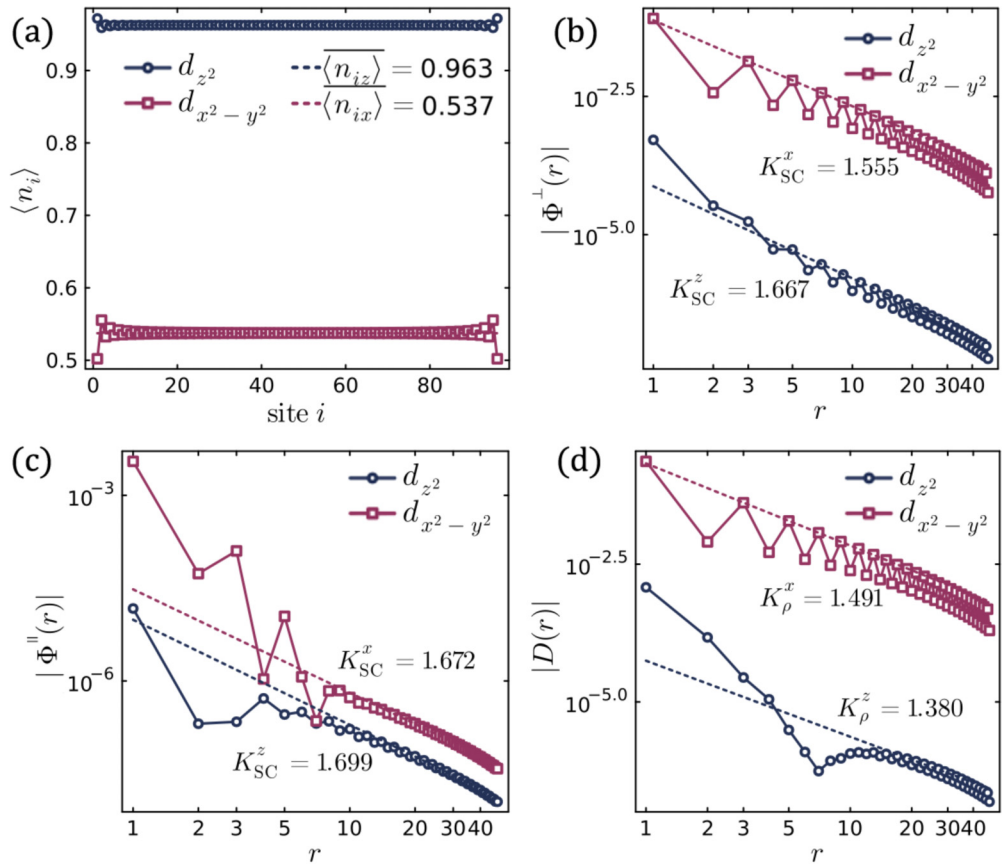

FIG. 10. DMRG simulated results of the order parameters at $J_H = 1$ eV. (a) The electron densities in the two E_g orbitals. (b) The interlayer singlet pairing correlation functions of each orbital. (c) The intralayer singlet pairing correlation functions. All of the interlayer and intralayer singlet pairing correlation functions follow an algebraic decay. (d) The charge density correlation functions for each orbital, exhibiting algebraic decay.

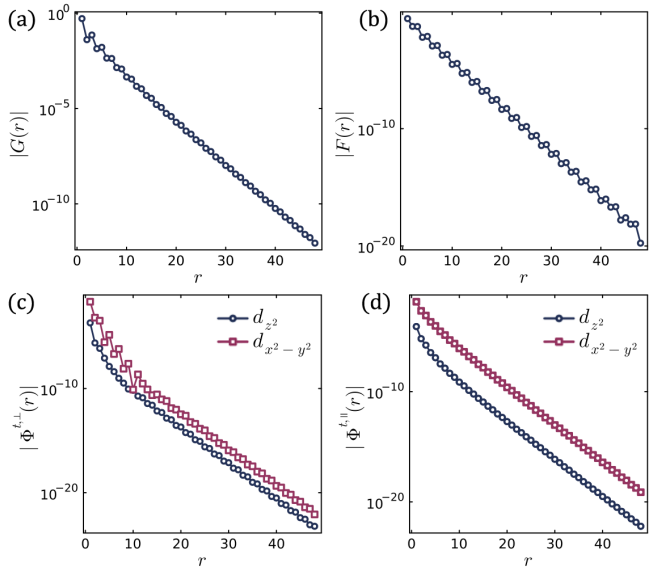

FIG. 11. DMRG results of the order parameters exhibiting exponential decay behaviors, simulated at $J_H = 1$ eV. (a) The single-particle correlation function $G(r)$. (b) The spin-spin correlation function $F(r)$. The interlayer (c) and intralayer (d) triplet pairing correlation functions across each orbital.

We also computed the interlayer and intralayer triplet pairing correlation functions, shown in Figs. 11(c) and 11(d). Both of these decay exponentially with distance. These results suggest the absence of the corresponding order parameters in the pressurized $La_3Ni_2O_7$ system, leaving singlet interlayer $3d_{x^2-y^2}$-orbital SC pairing as the dominant low-energy phenomena.

More DMRG results on the convergence of the pairing correlation functions and on the lattice of size $2 \times 2 \times 48$ are shown in Appendix D.

V. CONCLUSION AND DISCUSSION

In this work, we propose and study a bilayer two-orbital model for superconducting $La_3Ni_2O_7$ under high pressure, which fully accounts for the effects of the on-site triplet doublons. The results presented here provide significant insight into the interplay between Hund's coupling, electron correlation, and SC in the bilayer nickelate material. The underlying mother state is formed within a strong-coupling regime, characterized by robust Hund's coupling that leads to spin-triplet configurations for the two E_g orbitals in the Ni $3d^8$ electronic state. The strong interlayer superexchange interactions promote the formation of interlayer spin-1 singlet states, resulting in an interlayer VBS structure. When the system approaches the physically relevant Ni $d^{7.5}$ valence in

pressurized $La_3Ni_2O_7$, these spin-1 singlets gradually evolve into spin-$\frac{1}{2}$ singlets primarily involving the d_{z^2} orbitals. Doping introduces additional holes, which mediate phase coherence among these singlet bonds, eventually giving rise to SC.

The central finding of our work is the dominance of interlayer spinon singlet pairing across both the Hund's coupling (J_H) and doping regimes, suggesting that interlayer superexchange plays a pivotal role in stabilizing the superconducting state. This distinction points to the novelty of the superconducting mechanism in $La_3Ni_2O_7$, where the bilayer architecture, combined with the strong interlayer superexchange, offers a platform to explore unconventional SC. This structure fosters unique pairing mechanisms that rely heavily on the coupling between layers, distinguishing this system from the in-plane-dominated SC typically seen in cuprates and other layered systems.

Furthermore, our findings reveal that the coexistence of spin-1 and spin-$\frac{1}{2}$ singlets creates an unusual quantum entangled state that diverges from traditional models of SC. This entanglement between different spin channels suggests that both spin-1 and spin-$\frac{1}{2}$ singlets contribute to the overall pairing mechanism, raising fundamental questions about the precise nature of the superconducting phase in bilayer nickelates. The transition from a spin-1 valence bond solid to a mixed spin-1/spin-$\frac{1}{2}$ state, driven by doping, introduces the possibility of a rich and complex phase diagram. This phase diagram may exhibit a variety of superconducting properties, which is left for future work and may be experimentally clarified.

Note added. Recently, we became aware of unpublished work [102] that also considers an effective bilayer two-orbital t-J model incorporating strong Hund's coupling, similar to the model presented here. Our study builds upon such a model framework by performing detailed theoretical and numerical analyses (SPMF and DMRG) to investigate the nature of the SC pairing mechanism and symmetry.

ACKNOWLEDGMENTS

We are grateful to the stimulating discussions with Wei Li, Xing-Zhou Qu, and Jialin Chen. C.W. is supported by the National Natural Science Foundation of China under Grants No. 12234016 and No. 12174317. F.Y. is supported by the National Natural Science Foundation of China under Grant No. 12074031. C.L. is supported by the National Natural Science Foundation of China under Grant No. 12304180. Z.P. is supported by the National Natural Science Foundation of China under Grant No. 12504219. This work has been supported by the New Cornerstone Science Foundation.

DATA AVAILABILITY

The data supporting the findings of this study are available from the authors upon reasonable request.

APPENDIX A: DETAILS ON THE BILAYER t-J-J_H MODEL

In the second-order perturbation theory, the electron interactions are treated as zero-order terms while the kinetic terms are considered as first-order perturbations. Near the natural filling of $La_3Ni_2O_7$, the local Hilbert space at each site is constrained to the eight configurations shown in Fig. 2 in the strong correlation limit. The hole configuration (neither orbital is occupied) is important with two main considerations in mind: (i) It avoids unreasonable ferromagnetic superexchange terms, which take the form $-\frac{t^2}{V-J_H+\Delta\epsilon}$ in certain components of J; (ii) in the mean-field approach, the reservation of the hole configuration avoids momentum locking at zero, as the two orbitals are independent of each other without it. In addition, its reservation resulted in the zero-order terms in Hamiltonian (2) being partially retained in the resulting Hamiltonian (3).

The effects of the discarded high-energy subspace are captured through the superexchange terms, whose strength is determined by second-order perturbation theory. The intralayer superexchange parameters of the bilayer t-J-J_H model are related to the parameters of the original two-band Hubbard model through the following equations:

$$
\begin{aligned}
J^{\parallel}_{zz} &= \frac{4t^{\parallel 2}_{zz}}{U} + \frac{2t^{\parallel 2}_{zx}}{V+J_H+\epsilon_x-\epsilon_z}, \quad J^{\parallel}_{xx} = \frac{4t^{\parallel 2}_{xx}}{U} + \frac{2t^{\parallel 2}_{zx}}{V+J_H+\epsilon_z-\epsilon_x},\\
J^{\parallel}_{dd} &= \frac{t^{\parallel 2}_{zz}+t^{\parallel 2}_{xx}}{U+J_H} + t^{\parallel 2}_{zx}\left[\frac{1}{U+J_H+\epsilon_z-\epsilon_x}+\frac{1}{U+J_H+\epsilon_x-\epsilon_z}\right],\\
J^{\parallel}_{zx} &= \frac{t^{\parallel 2}_{zz}+t^{\parallel 2}_{xx}}{V+J_H} + 2t^{\parallel 2}_{zx}\left[\frac{1}{U+\epsilon_z-\epsilon_x}+\frac{1}{U+\epsilon_x-\epsilon_z}\right],\\
J^{\parallel}_{zd} &= t^{\parallel 2}_{zz}\left[\frac{1}{U+V}+\frac{1}{U-V+J_H}\right] + \frac{t^{\parallel 2}_{xx}}{4J_H} + \frac{t^{\parallel 2}_{zx}}{2}\frac{1}{2J_H+\epsilon_x-\epsilon_z}\\
&\quad + t^{\parallel 2}_{zx}\left[\frac{1}{U+V+\epsilon_x-\epsilon_z}+\frac{1}{U-V+J_H+\epsilon_z-\epsilon_x}\right],\\
J^{\parallel}_{xd} &= t^{\parallel 2}_{xx}\left[\frac{1}{U+V}+\frac{1}{U-V+J_H}\right] + \frac{t^{\parallel 2}_{zz}}{4J_H} + \frac{t^{\parallel 2}_{zx}}{2}\frac{1}{2J_H+\epsilon_z-\epsilon_x}\\
&\quad + t^{\parallel 2}_{zx}\left[\frac{1}{U+V+\epsilon_z-\epsilon_x}+\frac{1}{U-V+J_H+\epsilon_x-\epsilon_z}\right],
\end{aligned}
\tag{A1}
$$

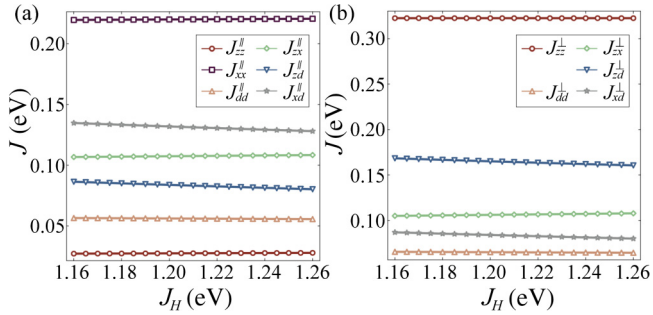

FIG. 12. (a) The intralayer superexchange parameters $J^{\parallel}$ and (b) the interlayer superexchange parameters $J^{\perp}$ as functions of Hund's coupling J_H.

and the interlayer parameters are as follows:

$$
\begin{aligned}
J_{zz}^{\perp} &= \frac{4t_{zz}^{\perp 2}}{U}, \quad J_{dd}^{\perp} = \frac{t_{zz}^{\perp 2}}{U+J_H}, \\
J_{zx}^{\perp} &= \frac{t_{zz}^{\perp 2}}{V+J_H}, \quad J_{xd}^{\perp} = \frac{t_{zz}^{\perp 2}}{4J_H}, \\
J_{zd}^{\perp} &= t_{zz}^{\perp 2}\left[\frac{1}{U+V}+\frac{1}{U-V+J_H}\right].
\end{aligned} \tag{A2}
$$

To visually show the trend of these parameters with J_H, we show the changes in these parameters within the range set in the SPMF method in Fig. 12.

Figure 12(a) shows how the intralayer superexchange parameters $J^{\parallel}$ vary with J_H, exhibiting that $J_{zz}^{\parallel}$, $J_{zx}^{\parallel}$ and the dominant parameter $J_{xx}^{\parallel}$ are positively correlated with J_H, while $J_{zd}^{\parallel}$, $J_{xd}^{\parallel}$, and $J_{dd}^{\parallel}$ are opposite. Similarly, the trend of the interlayer superexchange parameters $J^{\perp}$ with J_H is shown in Fig. 12(b), indicating that $J_{zx}^{\perp}$ is positively correlated with J_H, while $J_{zd}^{\parallel}$, $J_{xd}^{\parallel}$, and $J_{dd}^{\parallel}$ are opposite and the dominant parameter $J_{zz}^{\perp}$ is independent of J_H. The zero-order energies of some typical two-orbital configurations are shown in Fig. 13.

APPENDIX B: DETAILS OF THE SLAVE-PARTICLE THEORY

In the slave-particle mean-field approach, the spin-$\frac{1}{2}$ exchange interaction between two nearest-neighbor sites, labeled 1 and 2, can be conventionally decoupled into singlet hopping and pairing channels:

$$
\boldsymbol{S}_1 \cdot \boldsymbol{S}_2 = -\tfrac{3}{8}\chi_{12}^{\dagger}\chi_{12} - \tfrac{3}{8}\Delta_{12}^{\dagger}\Delta_{12},
$$

where hopping χ and pairing Δ are given as

$$
\chi_{12} = b_{1\uparrow}^{\dagger}b_{2\uparrow} + b_{1\downarrow}^{\dagger}b_{2\downarrow}, \quad \Delta_{12} = b_{1\downarrow}b_{2\uparrow} - b_{1\uparrow}b_{2\downarrow}.
$$

Here, the labels 1 and 2 are composite indices. For the interlayer d_{z^2} spin-$\frac{1}{2}$ interaction $J_{zz}^{\perp}\boldsymbol{S}_{itz}\cdot\boldsymbol{S}_{ibz}$, these indices represent (i,t,z) and (i,b,z), respectively, denoting site i, top (t) or bottom (b) layer, and the d_{z^2} orbital (labeled z). For the intralayer $d_{x^2-y^2}$ spin-$\frac{1}{2}$ interaction $J_{xx}^{\parallel}\boldsymbol{S}_{i\mu x}\cdot\boldsymbol{S}_{j\mu x}$, they represent (i,μ,x) and (j,μ,x), indicating sites i and j within the same layer μ and involving the $d_{x^2-y^2}$ orbital (labeled x). The operators $b_{s\sigma}$ ($b_{s\sigma}^{\dagger}$) annihilate (create) a slave boson for spin σ at composite site s.

Similarly, the interlayer spin-1 interaction $J_{dd}^{\perp}\boldsymbol{S}_{itd}\cdot\boldsymbol{S}_{ibd}$, involving E_g spin-1 moments on the top (t) and bottom (b) layers at site i, can also be decoupled into singlet channels. For this spin-1 exchange interaction, the situation is more involved. The spin state of two individual spin 1 moments can be denoted by $|m_1,m_2\rangle$, where $m_1,m_2\in\{+1,0,-1\}$ are the z-components of their respective spins. The combined two-spin states, denoted by $|J,M\rangle$ (where J is the total spin and M is its z-component), can be decomposed using Clebsch-Gordan coefficients into total spin-0 (singlet), spin-1 channel, and spin-2 channels. The total spin singlet $|J=0,M=0\rangle$ for two spin-1 entities, analogous to the spin-$\frac{1}{2}$ singlet state, is given by

$$
\left|\begin{matrix}0,\\ J\end{matrix}\ \begin{matrix}0\rangle\\ M\end{matrix}\right. = \frac{1}{\sqrt{3}}(|1,-1\rangle - |0,0\rangle + |-1,1\rangle).
$$

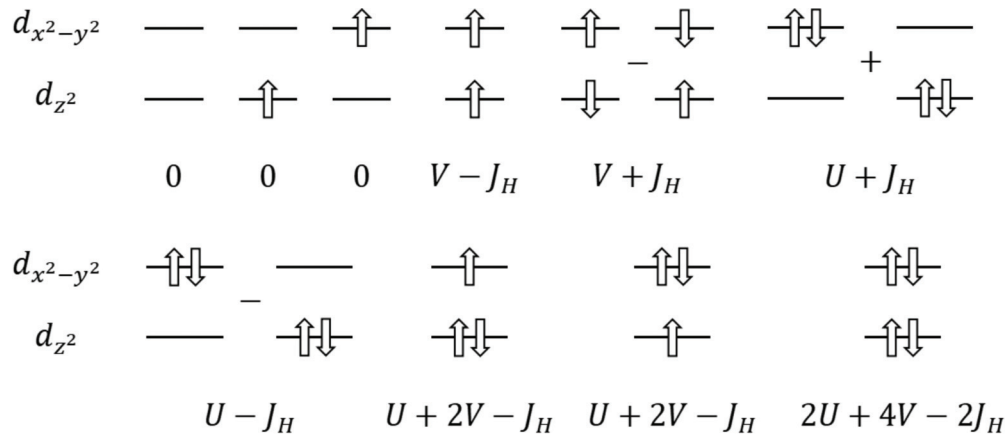

FIG. 13. The zero-order energies and the corresponding typical two-orbital configurations.

We define the total spin-singlet hopping and pairing operators using fermionic f-particles,

$$\Delta_0^\dagger = \frac{1}{\sqrt{3}}(f_{it,+1}^\dagger f_{id,-1}^\dagger - f_{it,0}^\dagger f_{id,0}^\dagger + f_{it,-1}^\dagger f_{id,+1}^\dagger),$$

$$\chi_0^\dagger = \frac{1}{\sqrt{3}}(f_{it,+1}^\dagger f_{id,+1} + f_{it,0}^\dagger f_{id,0} + f_{it,-1}^\dagger f_{id,-1}).$$

The mean-field decoupling of the spin-1 exchange interaction, when projected onto these total spin-singlet channels, is then given by

$$\boldsymbol{S}_{it} \cdot \boldsymbol{S}_{id} = -2\Delta_0^\dagger \Delta_0 - 2\chi_0^\dagger \chi_0.$$

In this decomposition, contributions from nonsinglet channels (i.e., $J = 1$ and 2) have been omitted, focusing on the formation of local singlets.

As highlighted in the main text, SC pairing can be conceptually understood as a quantum superposition of an "empty" electronic state and a "paired" electronic state. Focusing specifically on the "paired" state where four electrons occupy the E_g orbitals across a bilayer rung, a distinct pairing mechanism emerges. Initially, within each Ni ion, the intra-atomic Hund's rule dictates that the two E_g electrons (one in the $d_{x^2-y^2}$ orbital and one in the d_{z^2} orbital) will align their spins, forming a local spin-1 triplet state on each layer. Subsequently, these two local spin-1 moments, residing on the two layers of the rung, couple AFM via superexchange interaction, resulting in an interlayer spin-0 singlet state, as shown in the above $|\text{spin-1 singlet}\rangle \equiv |\underset{J}{0}, \underset{M}{0}\rangle$. Critically, this spin-1 mediated singlet configuration cannot be simply factorized into a direct product of two independent spin-$\frac{1}{2}$ singlet configurations, signifying a notable deviation from the conventional BCS theory of Cooper pairing.

In contrast, conventional electron singlet pairing in such a system would typically involve a spin configuration composed of two independent interlayer spin singlets, one formed by the $3d_{x^2-y^2}$ orbitals on the two layers and the other by the $3d_{z^2}$ orbitals. It is important to recognize that these two total spin-0 configurations—the spin-1 mediated singlet and the direct product of two spin-$\frac{1}{2}$ singlets—are not orthogonal. Mathematically, these configurations can be rearranged into two orthogonal total spin-0 states, reflecting the two distinct pathways to form a total spin-0 singlet from four spin-$\frac{1}{2}$ particles, as illustrated by the Clebsch-Gordan series decomposition $\frac{1}{2} \otimes \frac{1}{2} \otimes \frac{1}{2} \otimes \frac{1}{2} = (0 \oplus 1) \otimes (0 \oplus 1) = 0 \oplus 0 \oplus 1 \oplus 1 \oplus 1 \oplus 2$. To further elucidate the interlayer $3d_{x^2-y^2}$ singlet component originating from this spin-1 configuration, we acknowledge that the spin-1 state on each layer is a triplet formed by the combination of the $d_{x^2-y^2}$ and d_{z^2} electron spins, and the interlayer total spin singlet arises from the coupling of these two triplets. Projecting on the interlayer $3d_{x^2-y^2}$ spin-$\frac{1}{2}$ singlet channel $|3d_{x^2-y^2}\ \text{singlet}\rangle$, we can have $\langle 3d_{x^2-y^2}\ \text{singlet}|\text{spin-1 singlet}\rangle = \frac{\sqrt{3}}{2}$. In this sense, the physical $3d_{x^2-y^2}$ electron interlayer singlet pairing can be roughly given by

$$\Delta_x \propto \tilde{n}_z \langle \Delta_0 \rangle,$$

where $\tilde{n}_z$ arises from the holon condensation, leading to the phase coherence of the pairing.

APPENDIX C: RESULTS ON THE BILAYER TWO-ORBITAL HUBBARD MODEL

Figure 2 in the main text shows the eight configurations constituting the low-energy effective local Hilbert space of our bilayer t-J-J_H model. As analyzed in the main text and in Appendix A, the four spin-$\frac{1}{2}$ singlons with total particle number $N = 1$ and total spin $S = \frac{1}{2}$ (i.e., the configurations ② − ⑤ in Fig. 2) and the three spin-1 triplet doublons with $N = 2$ and $S = 1$ (i.e., the configurations ⑥ − ⑧ in Fig. 2) are the true low-energy configurations with U, V, and J_H as zero-order terms. The additional hole configuration with $N = 0$ and $S = 0$ (i.e., the configuration ① in Fig. 2) is retained due to the anomalous behavior of partial superexchange parameters and numerical necessity, which introduces the residual zero-order terms in Eq. (3) of the main text.

In this appendix, we solve the bilayer two-orbital Hubbard model combining Eqs. (1) and (2) using exact diagonalization and density matrix renormalization-group methods to demonstrate the validity of the perturbation theory by quantifying the ratios of the configurations ② − ⑧ in Fig. 2 in the ground state.

The results are shown in Fig. 14. Figure 14(a) shows the ratios of the configurations with different (N, S) in the ground state of the bilayer two-orbital Hubbard model with

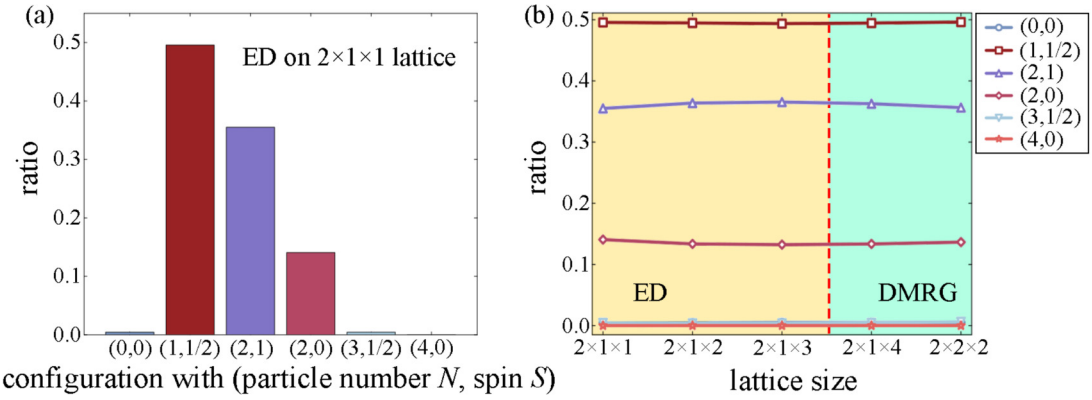

FIG. 14. (a) The ratios of configurations with total particle number N and total spin S in the ground state of the two-orbital Hubbard model on a $2 \times 1 \times 1$ lattice. (b) The ratios on lattices of different sizes.

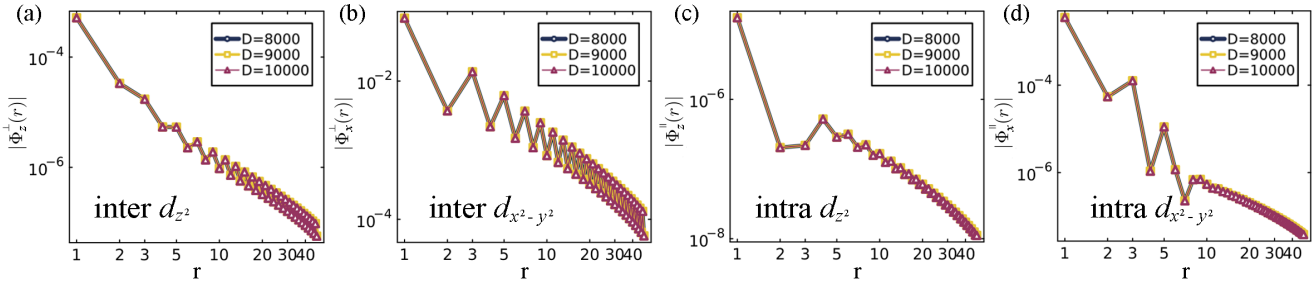

FIG. 15. The singlet pairing correlation functions calculated by DMRG with different bond dimensions D for (a) interlayer pairing in d_{z^2} orbitals, (b) interlayer pairing in $d_{x^2-y^2}$ orbitals, (c) intralayer pairing in d_{z^2} orbitals, and (d) intralayer pairing in $d_{x^2-y^2}$ orbitals.

the same parameter set of our bilayer t-J-J_H model ($J_H = 1$) on a $2 \times 1 \times 1$ lattice. Figure 14(b) displays the results on the lattices of different sizes, where we apply the exact diagonalization method on $2 \times 1 \times L_x$ lattices where $L_x = 1, 2, 3$, and the density matrix renormalization-group method is employed on $2 \times 1 \times 4$ and $2 \times 2 \times 2$ lattices. The results indicate that the spin-$\frac{1}{2}$ singlon and spin-1 triplet doublon are significantly dominant with a total ratio of about 0.87, exactly consistent with our analysis based on the perturbation theory.

APPENDIX D: MORE DMRG RESULTS ON THE BILAYER t-J-J_H MODEL

In this appendix, we provide more DMRG results, in particular on convergence verification and on the lattice of size $2 \times 2 \times 48$.

Figure 15 exhibits the singlet pairing correlation functions calculated by DMRG with different bond dimensions D for (a) interlayer pairing in d_{z^2} orbitals, (b) interlayer pairing in $d_{x^2-y^2}$ orbitals, (c) intralayer pairing in d_{z^2} orbitals, and (d) intralayer pairing in $d_{x^2-y^2}$ orbitals. The results show that these pairing correlation functions highly overlap in the bond dimensions $D = 8000$, 9000, and 10 000, indicating that our DMRG results have converged with $D = 10\,000$.

Furthermore, we also solve the bilayer t-J-J_H model by DMRG on a $2 \times 2 \times 48$ lattice with $J_H = 1$ and the same set of other parameters on the $2 \times 1 \times 96$ ladder, retaining up to $D = 10\,000$ $\mathrm{U(1)_{charge}} \times \mathrm{SU(2)_{spin}}$ multiplets as well. The new results are shown in Fig. 16. Figure 16(a) exhibits the interlayer singlet pairing correlation functions, while Fig. 16(b) shows the intralayer one. Although arithmetic constraints prevent us from extending D enough to observe the algebraic decay of the pairing correlation functions over the full distance we examine, the dominance of the interlayer $d_{x^2-y^2}$ pairing can still be determined from the dominant amplitude and the slowest algebraic decay rate fitted in a small range, which is qualitatively consistent with our SPMF results on a two-dimensional bilayer square lattice and the DMRG results on the $2 \times 1 \times 96$ ladder. In addition, the result in the $2 \times 2 \times 64$ lattice that the SC exponents are larger than 2, different from the ones in $2 \times 1 \times 128$, is likely due to the finite-size effect. We predict that our two-orbital model may also support SC exponents smaller than 2 in a lattice with width equal to or larger than 3, which implies the existence of SC in exact 2D systems, as our SPMF results show.

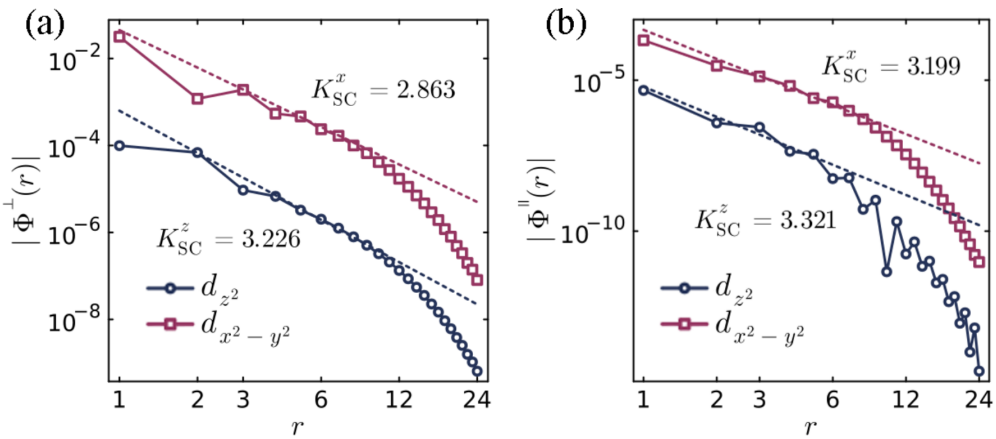

FIG. 16. The DMRG results on a $2 \times 2 \times 48$ lattice. (a) The interlayer singlet pairing correlation functions. (b) The intralayer singlet pairing correlation functions.

[1] H. Sun, M. Huo, X. Hu, J. Li, Z. Liu, Y. Han, L. Tang, Z. Mao, P. Yang, B. Wang, J. Cheng, D.-X. Yao, G.-M. Zhang, and M. Wang, Signatures of superconductivity near 80 K in a nickelate under high pressure, Nature (London) **621**, 493 (2023).

[2] Y. Zhang, D. Su, Y. Huang, Z. Shan, H. Sun, M. Huo, K. Ye, J. Zhang, Z. Yang, Y. Xu, Y. Su, R. Li, M. Smidman, M. Wang, L. Jiao, and H. Yuan, High-temperature superconductivity with zero resistance and strange-metal behavior in $La_3Ni_2O_{7-\delta}$, Nat. Phys. **20**, 1269 (2024).

[3] J. Hou, P.-T. Yang, Z.-Y. Liu, J.-Y. Li, P.-F. Shan, L. Ma, G. Wang, N.-N. Wang, H.-Z. Guo, J.-P. Sun, Y. Uwatoko, M. Wang, G.-M. Zhang, B.-S. Wang, and J.-G. Cheng, Emergence of high-temperature superconducting phase in pressurized $La_3Ni_2O_7$ crystals, Chin. Phys. Lett. **40**, 117302 (2023).

[4] G. Wang, N. N. Wang, X. L. Shen, J. Hou, L. Ma, L. F. Shi, Z. A. Ren, Y. D. Gu, H. M. Ma, P. T. Yang, Z. Y. Liu, H. Z. Guo, J. P. Sun, G. M. Zhang, S. Calder, J.-Q. Yan, B. S. Wang, Y. Uwatoko, and J.-G. Cheng, Pressure-induced superconductivity in polycrystalline $La_3Ni_2O_7$, Phys. Rev. X **14**, 011040 (2024).

[5] G. Wang, N. Wang, Y. Wang, L. Shi, X. Shen, J. Hou, H. Ma, P. Yang, Z. Liu, H. Zhang, X. Dong, J. Sun, B. Wang, K. Jiang, J. Hu, Y. Uwatoko, and J. Cheng, Observation of high-temperature superconductivity in the high-pressure tetragonal phase of $La_2PrNi_2O_{7-\delta}$, arXiv:2311.08212.

[6] M. Zhang, C. Pei, Q. Wang, Y. Zhao, C. Li, W. Cao, S. Zhu, J. Wu, and Y. Qi, Effects of pressure and doping on Ruddlesden-Popper phases $La_{n+1}Ni_nO_{3n+1}$, J. Mater. Sci. Technol. **185**, 147 (2024).

[7] Y. Zhou, J. Guo, S. Cai, H. Sun, C. Li, J. Zhao, P. Wang, J. Han, X. Chen, Y. Chen, Q. Wu, Y. Ding, T. Xiang, H.-k. Mao, and L. Sun, Investigations of key issues on the reproducibility of high-T_c superconductivity emerging from compressed $La_3Ni_2O_7$, Matter Radiat. Extremes **10**, 027801 (2025).

[8] N. Wang, G. Wang, X. Shen, J. Hou, J. Luo, X. Ma, H. Yang, L. Shi, J. Dou, J. Feng, J. Yang, Y. Shi, Z. Ren, H. Ma, P. Yang, Z. Liu, Y. Liu, H. Zhang, X. Dong, Y. Wang *et al.*, Bulk high-temperature superconductivity in the high-pressure tetragonal phase of bilayer $La_2PrNi_2O_7$, Nature (London) **634**, 579 (2024).

[9] J. Li, D. Peng, P. Ma, H. Zhang, Z. Xing, X. Huang, C. Huang, M. Huo, D. Hu, Z. Dong, X. Chen, T. Xie, H. Dong, H. Sun, Q. Zeng, H.-k. Mao, and M. Wang, Identification of the superconductivity in bilayer nickelate $La_3Ni_2O_7$ upon 100 GPa, Natl. Sci. Rev. **12**, nwaf220 (2025).

[10] Y. Ueki, H. Sakurai, H. Nagata, K. Yamane, R. Matsumoto, K. Terashima, K. Hirose, H. Ohta, M. Kato, and Y. Takano, Phase diagram of pressure-induced high temperature superconductor $La_3Ni_2O_{7+\delta}$, J. Phys. Soc. Jpn. **94**, 013703 (2025).

[11] T. Fukamachi, Y. Kobayashi, T. Miyashita, and M. Sato, ^{139}La NMR studies of layered perovskite systems $La_3Ni_2O_{7-\delta}$ and $La_4Ni_3O_{10}$, J. Phys. Chem. Solids **62**, 195 (2001).

[12] Z. Liu, H. Sun, M. Huo, X. Ma, Y. Ji, E. Yi, L. Li, H. Liu, J. Yu, Z. Zhang, Z. Chen, F. Liang, H. Dong, H. Guo, D. Zhong, B. Shen, S. Li, and M. Wang, Evidence for charge and spin density waves in single crystals of $La_3Ni_2O_7$ and $La_3Ni_2O_6$, Sci. China Phys. Mech. Astron. **66**, 217411 (2023).

[13] L. Wang, Y. Li, S. Xie, F. Liu, H. Sun, C. Huang, Y. Gao, T. Nakagawa, B. Fu, B. Dong, Z. Cao, R. Yu, S. I. Kawaguchi, H. Kadobayashi, M. Wang, C. Jin, H. Kwang Mao, and H. Liu, Structure responsible for the superconducting state in $La_3Ni_2O_7$ at low temperature and high pressure conditions, J. Am. Chem. Soc. **146**, 7506 (2024).

[14] X. Chen, J. Choi, Z. Jiang, J. Mei, K. Jiang, J. Li, S. Agrestini, M. Garcia-Fernandez, X. Huang, H. Sun, D. Shen, M. Wang, J. Hu, Y. Lu, K.-J. Zhou, and D. Feng, Electronic and magnetic excitations in $La_3Ni_2O_7$, Nat. Commun. **15**, 9597 (2024).

[15] M. Kakoi, T. Oi, Y. Ohshita, M. Yashima, K. Kuroki, T. Kato, H. Takahashi, S. Ishiwata, Y. Adachi, N. Hatada, T. Uda, and H. Mukuda, Multiband metallic ground state in multilayered nickelates $La_3Ni_2O_7$ and $La_4Ni_3O_{10}$ probed by ^{139}La-NMR at ambient pressure, J. Phys. Soc. Jpn. **93**, 053702 (2024).

[16] T. Xie, M. Huo, X. Ni, F. Shen, X. Huang, H. Sun, H. C. Walker, D. Adroja, D. Yu, B. Shen, L. He, K. Cao, and M. Wang, Strong interlayer magnetic exchange coupling in $La_3Ni_2O_{7-\delta}$ revealed by inelastic neutron scattering, Sci. Bull. **69**, 3221 (2024).

[17] J.-J. Feng, T. Han, J.-P. Song, M.-S. Long, X.-Y. Hou, C.-J. Zhang, Q.-G. Mu, and L. Shan, Unaltered density wave transition and pressure-induced signature of superconductivity in Nd-doped $La_3Ni_2O_7$, Phys. Rev. B **110**, L100507 (2024).

[18] Y. Meng, Y. Yang, H. Sun, S. Zhang, J. Luo, L. Chen, X. Ma, M. Wang, F. Hong, X. Wang, and X. Yu, Density-wave-like gap evolution in $La_3Ni_2O_7$ under high pressure revealed by ultrafast optical spectroscopy, Nat. Commun. **15**, 10408 (2024).

[19] S. Fan, Z. Luo, M. Huo, Z. Wang, H. Li, H. Yang, M. Wang, D.-X. Yao, and H.-H. Wen, Tunneling spectra with gaplike features observed in nickelate $La_3Ni_2O_7$ at ambient pressure, Phys. Rev. B **110**, 134520 (2024).

[20] Y. Li, Y. Cao, L. Liu, P. Peng, H. Lin, C. Pei, M. Zhang, H. Wu, X. Du, W. Zhao, K. Zhai, X. Zhang, J. Zhao, M. Lin, P. Tan, Y. Qi, G. Li, H. Guo, L. Yang, and L. Yang, Distinct ultrafast dynamics of bilayer and trilayer nickelate superconductors regarding the density-wave-like transitions, Sci. Bull. **70**, 180 (2025).

[21] Z. Liu, M. Huo, J. Li, Q. Li, Y. Liu, Y. Dai, X. Zhou, J. Hao, Y. Lu, M. Wang, and H.-H. Wen, Electronic correlations and partial gap in the bilayer nickelate $La_3Ni_2O_7$, Nat. Commun. **15**, 7570 (2024).

[22] M. Wang, H.-H. Wen, T. Wu, D.-X. Yao, and T. Xiang, Normal and superconducting properties of $La_3Ni_2O_7$, Chin. Phys. Lett. **41**, 077402 (2024).

[23] J. Yang, H. Sun, X. Hu, Y. Xie, T. Miao, H. Luo, H. Chen, B. Liang, W. Zhu, G. Qu, C.-Q. Chen, M. Huo, Y. Huang, S. Zhang, F. Zhang, F. Yang, Z. Wang, Q. Peng, H. Mao, G. Liu *et al.*, Orbital-dependent electron correlation in double-layer nickelate $La_3Ni_2O_7$, Nat. Commun. **15**, 4373 (2024).

[24] Y. Li, X. Du, Y. Cao, C. Pei, M. Zhang, W. Zhao, K. Zhai, R. Xu, Z. Liu, Z. Li, J. Zhao, G. Li, Y. Qi, H. Guo, Y. Chen, and L. Yang, Electronic correlation and pseudogap-like behavior of high-temperature superconductor $La_3Ni_2O_7$, Chin. Phys. Lett. **41**, 087402 (2024).

[25] H.-Y. Zhang, Y.-J. Bai, F.-J. Kong, X.-Q. Wu, Y.-H. Xing, and N. Xu, Doping evolution of the normal state magnetic excitations in pressurized $La_3Ni_2O_7$, New J. Phys. **26**, 123027 (2024).

[26] Y. Liu, M. Ou, H. Chu, H. Yang, Q. Li, Y.-J. Zhang, and H.-H. Wen, Growth and characterization of the $La_3Ni_2O_{7-\delta}$ thin films: Dominant contribution of the $d_{x^2-y^2}$ orbital at ambient pressure, Phys. Rev. Mater. **8**, 124801 (2024).

[27] K. Chen, X. Liu, J. Jiao, M. Zou, C. Jiang, X. Li, Y. Luo, Q. Wu, N. Zhang, Y. Guo, and L. Shu, Evidence of spin density waves in $La_3Ni_2O_{7-\delta}$, Phys. Rev. Lett. **132**, 256503 (2024).

[28] N. K. Gupta, R. Gong, Y. Wu, M. Kang, C. T. Parzyck, B. Z. Gregory, N. Costa, R. Sutarto, S. Sarker, A. Singer, D. G. Schlom, K. M. Shen, and D. G. Hawthorn, Anisotropic spin stripe domains in bilayer $La_3Ni_2O_7$, Nat. Commun. **16**, 6560 (2025).

[29] M. Xu, G. C. Jose, A. Rutherford, H. Wang, S. Zhang, R. J. Cava, H. Zhou, W. Bi, and W. Xie, Pressure-induced phase transitions in bilayer $La_3Ni_2O_7$, arXiv:2410.18840.

[30] M. Li, Y. Wang, C. Pei, M. Zhang, N. Li, J. Guan, M. Amboage, N.-D. Adama, Q. Kong, Y. Qi, and W. Yang, Distinguishing electronic band structure of single-layer and bilayer Ruddlesden-Popper nickelates probed by *in-situ* high pressure x-ray absorption near-edge spectroscopy, arXiv:2410.04230.

[31] X. Zhou, W. He, Z. Zhou, K. Ni, M. Huo, D. Hu, Y. Zhu, E. Zhang, Z. Jiang, S. Zhang, S. Su, J. Jiang, Y. Yan, Y. Wang, D. Shen, X. Liu, J. Zhao, M. Wang, M. Liu, Z. Du *et al.*, Revealing nanoscale structural phase separation in $La_3Ni_2O_{7-\delta}$ single crystal via scanning near-field optical microscopy, arXiv:2410.06602.

[32] B. Su, C. Huang, J. Zhao, M. Huo, J. Luo, M. Wang, and Z.-G. Chen, Strongly anisotropic charge dynamics in $La_3Ni_2O_7$ with coherent-to-incoherent crossover of interlayer charge dynamics, arXiv:2411.10786.

[33] E. Mijit, P. Ma, C. J. Sahle, A. D. Rosa, Z. Hu, F. De Angelis, A. Lopez, S. Amatori, G. Tchoudinov, Y. Joly, T. Irifune, J. E. F. S. Rodrigues, G. Garbarino, S. G. Parra, M. Wang, R. Yu, and O. Mathon, Local electronic properties of $La_3Ni_2O_7$ under pressure, arXiv:2412.08269.

[34] X. Ren, R. Sutarto, X. Wu, J. Zhang, H. Huang, T. Xiang, J. Hu, R. Comin, X. Zhou, and Z. Zhu, Resolving the electronic ground state of $La_3Ni_2O_{7-\delta}$ films, Commun. Phys. **8**, 52 (2025).

[35] R. Khasanov, T. J. Hicken, D. J. Gawryluk, V. Sazgari, I. Plokhikh, L. P. Sorel, M. Bartkowiak, S. Bötzel, F. Lechermann, I. M. Eremin, H. Luetkens, and Z. Guguchia, Pressure-enhanced splitting of density wave transitions in $La_3Ni_2O_{7-\delta}$, Nat. Phys. **21**, 430 (2025).

[36] D. Zhao, Y. Zhou, M. Huo, Y. Wang, L. Nie, Y. Yang, J. Ying, M. Wang, T. Wu, and X. Chen, Pressure-enhanced spin-density-wave transition in double-layer nickelate $La_3Ni_2O_{7-\delta}$, Sci. Bull. **70**, 1239 (2025).

[37] B. Chen, H. Zhang, J. Li, D. Hu, M. Huo, S. Wang, C. Xi, Z. Wang, H. Sun, M. Wang, and B. Shen, Unveiling the multiband metallic nature of the normal state in the nickelate $La_3Ni_2O_7$, Phys. Rev. B **111**, 054519 (2025).

[38] M. Shi, D. Peng, Y. Li, Z. Xing, Y. Wang, K. Fan, H. Li, R. Wu, Z. Zeng, Q. Zeng, J. Ying, and X. Chen, Prerequisite of superconductivity: SDW rather than tetragonal structure in double-layer $La_3Ni_2O_{7-\delta}$, arXiv:2501.14202.

[39] F. Li, Z. Xing, D. Peng, J. Dou, N. Guo, L. Ma, Y. Zhang, L. Wang, J. Luo, J. Yang, J. Zhang, T. Chang, Y.-S. Chen, W. Cai, J. Cheng, Y. Wang, Z. Zeng, Q. Zheng, R. Zhou, Q. Zeng *et al.*, Ambient pressure growth of bilayer nickelate single crystals with superconductivity over 90 K under high pressure, arXiv:2501.14584.

[40] M. Huo, P. Ma, C. Huang, X. Huang, H. Sun, and M. Wang, Low volume fraction of high-T_c superconductivity in $La_3Ni_2O_7$ at 80 K and ambient pressure, arXiv:2501.15929.

[41] Y. Zhang, C. Pei, N. Guo, L. Fan, M. Zhang, L. Wang, G. Zhang, F. Li, Y. Wang, C. Ma, W. Cheng, S. Wang, Q. Zheng, Y. Qi, and J. Zhang, Strong oxidizing annealing of bilayer La3Ni2O7- results in suppression of superconductivity under high pressure, J. Solid State Chem. **355**, 125757 (2026).

[42] Z. Luo, X. Hu, M. Wang, W. Wú, and D.-X. Yao, Bilayer two-orbital model of $La_3Ni_2O_7$ under pressure, Phys. Rev. Lett. **131**, 126001 (2023).

[43] D. A. Shilenko and I. V. Leonov, Correlated electronic structure, orbital-selective behavior, and magnetic correlations in double-layer $La_3Ni_2O_7$ under pressure, Phys. Rev. B **108**, 125105 (2023).

[44] H. LaBollita, V. Pardo, M. R. Norman, and A. S. Botana, Electronic structure and magnetic properties of $La_3Ni_2O_7$ under pressure: Active role of the Ni-$d_{x^2-y^2}$ orbitals, arXiv:2309.17279.

[45] Q.-G. Yang, D. Wang, and Q.-H. Wang, Possible $S_{\pm}$-wave superconductivity in $La_3Ni_2O_7$, Phys. Rev. B **108**, L140505 (2023).

[46] V. Christiansson, F. Petocchi, and P. Werner, Correlated electronic structure of $La_3Ni_2O_7$ under pressure, Phys. Rev. Lett. **131**, 206501 (2023).

[47] H. Oh and Y.-H. Zhang, Type-II t-J model and shared superexchange coupling from Hund's rule in superconducting $La_3Ni_2O_7$, Phys. Rev. B **108**, 174511 (2023).

[48] X. Sui, X. Han, H. Jin, X. Chen, L. Qiao, X. Shao, and B. Huang, Electronic properties of the bilayer nickelates $R_3Ni_2O_7$ with oxygen vacancies (R=La or Ce), Phys. Rev. B **109**, 205156 (2024).

[49] Y. Zhang, L.-F. Lin, A. Moreo, and E. Dagotto, Electronic structure, dimer physics, orbital-selective behavior, and magnetic tendencies in the bilayer nickelate superconductor $La_3Ni_2O_7$ under pressure, Phys. Rev. B **108**, L180510 (2023).

[50] J. Huang, Z. D. Wang, and T. Zhou, Impurity and vortex states in the bilayer high-temperature superconductor $La_3Ni_2O_7$, Phys. Rev. B **108**, 174501 (2023).

[51] Y. Shen, M. Qin, and G.-M. Zhang, Effective Bi-layer model Hamiltonian and density-matrix renormalization group study for the high-T_c superconductivity $La_3Ni_2O_7$ under high pressure, Chin. Phys. Lett. **40**, 127401 (2023).

[52] Y.-F. Yang, G.-M. Zhang, and F.-C. Zhang, Interlayer valence bonds and two-component theory for high-T_c superconductivity of $La_3Ni_2O_7$ under pressure, Phys. Rev. B **108**, L201108 (2023).

[53] Q. Qin and Y.-F. Yang, High-T_c superconductivity by mobilizing local spin singlets and possible route to higher T_c in pressurized $La_3Ni_2O_7$, Phys. Rev. B **108**, L140504 (2023).

[54] Y.-B. Liu, J.-W. Mei, F. Ye, W.-Q. Chen, and F. Yang, $S^{\pm}$-wave pairing and the destructive role of apical-oxygen deficiencies in $La_3Ni_2O_7$ under pressure, Phys. Rev. Lett. **131**, 236002 (2023).

[55] F. Lechermann, J. Gondolf, S. Bötzel, and I. M. Eremin, Electronic correlations and superconducting instability in $La_3Ni_2O_7$ under high pressure, Phys. Rev. B **108**, L201121 (2023).

[56] H. Sakakibara, N. Kitamine, M. Ochi, and K. Kuroki, Possible high T_c superconductivity in $La_3Ni_2O_7$ under high pressure through manifestation of a nearly half-filled bilayer Hubbard model, Phys. Rev. Lett. **132**, 106002 (2024).

[57] Y. Gu, C. Le, Z. Yang, X. Wu, and J. Hu, Effective model and pairing tendency in the bilayer Ni-based superconductor $La_3Ni_2O_7$, Phys. Rev. B **111**, 174506 (2025).

[58] C. Lu, Z. Pan, F. Yang, and C. Wu, Interlayer-coupling-driven high-temperature superconductivity in $La_3Ni_2O_7$ under pressure, Phys. Rev. Lett. **132**, 146002 (2024).

[59] Z. Liao, L. Chen, G. Duan, Y. Wang, C. Liu, R. Yu, and Q. Si, Electron correlations and superconductivity in $La_3Ni_2O_7$ under pressure tuning, Phys. Rev. B **108**, 214522 (2023).

[60] X.-Z. Qu, D.-W. Qu, J. Chen, C. Wu, F. Yang, W. Li, and G. Su, Bilayer t-J-$J_\perp$ model and magnetically mediated pairing in the pressurized nickelate $La_3Ni_2O_7$, Phys. Rev. Lett. **132**, 036502 (2024).

[61] K. Jiang, Z. Wang, and F.-C. Zhang, High temperature superconductivity in $La_3Ni_2O_7$, Chin. Phys. Lett. **41**, 017402 (2024).

[62] Y. Zhang, L.-F. Lin, A. Moreo, T. A. Maier, and E. Dagotto, Trends in electronic structures and $s_\pm$-wave pairing for the rare-earth series in bilayer nickelate superconductor $R_3Ni_2O_7$, Phys. Rev. B **108**, 165141 (2023).

[63] X.-Z. Qu, D.-W. Qu, W. Li, and G. Su, Hund's rule, interorbital hybridization, and high-Tc superconductivity in the bilayer nickelate $La_3Ni_2O_7$, Phys. Rev. B **112**, L161101 (2025).

[64] R. Jiang, J. Hou, Z. Fan, Z.-J. Lang, and W. Ku, Pressure driven fractionalization of ionic spins results in cupratelike high-T_c superconductivity in $La_3Ni_2O_7$, Phys. Rev. Lett. **132**, 126503 (2024).

[65] D.-C. Lu, M. Li, Z.-Y. Zeng, W. Hou, J. Wang, F. Yang, and Y.-Z. You, Superconductivity from doping symmetric mass generation insulators: Application to $La_3Ni_2O_7$ under pressure, arXiv:2308.11195.

[66] N. Kitamine, M. Ochi, and K. Kuroki, Theoretical designing of multiband nickelate and palladate superconductors with $d^{8+\delta}$ configuration, arXiv:2308.12750.

[67] J.-X. Zhang, H.-K. Zhang, Y.-Z. You, and Z.-Y. Weng, Strong pairing originated from an emergent $\mathbb{Z}_2$ Berry phase in $La_3Ni_2O_7$, Phys. Rev. Lett. **133**, 126501 (2024).

[68] Z. Pan, C. Lu, F. Yang, and C. Wu, Effect of rare-earth element substitution in superconducting $R_3Ni_2O_7$ under pressure, Chin. Phys. Lett. **41**, 087401 (2024).

[69] H. Sakakibara, M. Ochi, H. Nagata, Y. Ueki, H. Sakurai, R. Matsumoto, K. Terashima, K. Hirose, H. Ohta, M. Kato, Y. Takano, and K. Kuroki, Theoretical analysis on the possibility of superconductivity in the trilayer Ruddlesden-Popper nickelate $La_4Ni_3O_{10}$ under pressure and its experimental examination: Comparison with $La_3Ni_2O_7$, Phys. Rev. B **109**, 144511 (2024).

[70] H. Lange, L. Homeier, E. Demler, U. Schollwöck, A. Bohrdt, and F. Grusdt, Pairing dome from an emergent Feshbach resonance in a strongly repulsive bilayer model, Phys. Rev. B **110**, L081113 (2024).

[71] H. Yang, H. Oh, and Y.-H. Zhang, Strong pairing from a small Fermi surface beyond weak coupling: Application to $La_3Ni_2O_7$, Phys. Rev. B **110**, 104517 (2024).

[72] H. Schlömer, U. Schollwöck, F. Grusdt, and A. Bohrdt, Superconductivity in the pressurized nickelate $La_3Ni_2O_7$ in the vicinity of a BEC-BCS crossover, Commun. Phys. **7**, 366 (2024).

[73] H. Lange, L. Homeier, E. Demler, U. Schollwöck, F. Grusdt, and A. Bohrdt, Feshbach resonance in a strongly repulsive ladder of mixed dimensionality: A possible scenario for bilayer nickelate superconductors, Phys. Rev. B **109**, 045127 (2024).

[74] Z. Fan, J.-F. Zhang, B. Zhan, D. Lv, X.-Y. Jiang, B. Normand, and T. Xiang, Superconductivity in nickelate and cuprate superconductors with strong bilayer coupling, Phys. Rev. B **110**, 024514 (2024).

[75] Y. Cao and Y. F. Yang, Flat bands promoted by Hund's rule coupling in the candidate double-layer high-temperature superconductor $La_3Ni_2O_7$ under high pressure, Phys. Rev. B **109**, L081105 (2024).

[76] Y. Zhang, L.-F. Lin, A. Moreo, T. A. Maier, and E. Dagotto, Structural phase transition, $s_\pm$-wave pairing, and magnetic stripe order in bilayered superconductor $La_3Ni_2O_7$ under pressure, Nat. Commun. **15**, 2470 (2024).

[77] B. Geisler, J. J. Hamlin, G. R. Stewart, R. G. Hennig, and P. Hirschfeld, Structural transitions, octahedral rotations, and electronic properties of $A_3Ni_2O_7$ rare-earth nickelates under high pressure, npj Quantum Mater. **9**, 38 (2024).

[78] L. C. Rhodes and P. Wahl, Structural routes to stabilize superconducting $La_3Ni_2O_7$ at ambient pressure, Phys. Rev. Mater. **8**, 044801 (2024).

[79] Y. Zhang, L.-F. Lin, A. Moreo, T. A. Maier, and E. Dagotto, Electronic structure, magnetic correlations, and superconducting pairing in the reduced Ruddlesden-Popper bilayer $La_3Ni_2O_6$ under pressure: Different role of $d_{3z^2-r^2}$ orbital compared with $La_3Ni_2O_7$, Phys. Rev. B **109**, 045151 (2024).

[80] B. Geisler, L. Fanfarillo, J. J. Hamlin, G. R. Stewart, R. G. Hennig, and P. J. Hirschfeld, Optical properties and electronic correlations in $La_3Ni_2O_{7-\delta}$ bilayer nickelates under high pressure, npj Quantum Mater. **9**, 89 (2024).

[81] Y.-H. Tian, Y. Chen, J.-M. Wang, R.-Q. He, and Z.-Y. Lu, Correlation effects and concomitant two-orbital $s_\pm$-wave superconductivity in $La_3Ni_2O_7$ under high pressure, Phys. Rev. B **109**, 165154 (2024).

[82] Z. Luo, B. Lv, M. Wang, W. Wú, and D.-X. Yao, High-T_c superconductivity in $La_3Ni_2O_7$ based on the bilayer two-orbital t-j model, npj Quantum Mater. **9**, 61 (2024).

[83] T. Kaneko, H. Sakakibara, M. Ochi, and K. Kuroki, Pair correlations in the two-orbital Hubbard ladder: Implications for superconductivity in the bilayer nickelate $La_3Ni_2O_7$, Phys. Rev. B **109**, 045154 (2024).

[84] W. Wú, Z. Luo, D.-X. Yao, and M. Wang, Superexchange and charge transfer in the nickelate superconductor $La_3Ni_2O_7$ under pressure, Sci. China Phys. Mech. Astron. **67**, 117402 (2024).

[85] Y.-F. Yang, Decomposition of multilayer superconductivity with interlayer pairing, Phys. Rev. B **110**, 104507 (2024).

[86] C. Lu, Z. Pan, F. Yang, and C. Wu, Interplay of two E_g orbitals in superconducting $La_3Ni_2O_7$ under pressure, Phys. Rev. B **110**, 094509 (2024).

[87] J. Chen, F. Yang, and W. Li, Orbital-selective superconductivity in the pressurized bilayer nickelate $La_3Ni_2O_7$: An infinite projected entangled-pair state study, Phys. Rev. B **110**, L041111 (2024).

[88] M. Kakoi, T. Kaneko, H. Sakakibara, M. Ochi, and K. Kuroki, Pair correlations of the hybridized orbitals in a ladder model for the bilayer nickelate $La_3Ni_2O_7$, Phys. Rev. B **109**, L201124 (2024).

[89] E. Talantsev and V. Chistyakov, Debye temperature, electron-phonon coupling constant, and three-dome shape of crystalline strain as a function of pressure in highly compressed $La_3Ni_2O_{7-\delta}$, Lett. Mater. **14**, 262 (2024).

[90] Z. Ouyang, M. Gao, and Z.-Y. Lu, Absence of electron-phonon coupling superconductivity in the bilayer phase of $La_3Ni_2O_7$ under pressure, npj Quantum Mater. **9**, 80 (2024).

[91] X. Wu, H. Yang, and Y.-H. Zhang, Deconfined Fermi liquid to Fermi liquid transition and superconducting instability, Phys. Rev. B **110**, 125122 (2024).

[92] Y. Zhang, L.-F. Lin, A. Moreo, T. A. Maier, and E. Dagotto, Electronic structure, self-doping, and superconducting instability in the alternating single-layer trilayer stacking nickelates $La_3Ni_2O_7$, Phys. Rev. B **110**, L060510 (2024).

[93] G. Heier, K. Park, and S. Y. Savrasov, Competing d_{xy} and $s_{\pm}$ pairing symmetries in superconducting $La_3Ni_2O_7$: LDA + FLEX Calculations, Phys. Rev. B **109**, 104508 (2024).

[94] H. Oh, H. Yang, and Y.-H. Zhang, High-temperature superconductivity from kinetic energy, arXiv:2411.07292.

[95] Z. Wang, K. Jiang, and F.-C. Zhang, Self-doped molecular mott insulator for bilayer high-temperature superconducting $La_3Ni_2O_7$, arXiv:2412.18469.

[96] H.-X. Xu and D. Guterding, Incommensurate spin-fluctuations and competing pairing symmetries in $La_3Ni_2O_7$, Phys. Rev. B **112**, 174519 (2025).

[97] S. Ryee, N. Witt, and T. O. Wehling, Quenched pair breaking by interlayer correlations as a key to superconductivity in $La_3Ni_2O_7$, Phys. Rev. Lett. **133**, 096002 (2024).

[98] X. Chen, P. Jiang, J. Li, Z. Zhong, and Y. Lu, Charge and spin instabilities in superconducting $La_3Ni_2O_7$, Phys. Rev. B **111**, 014515 (2025).

[99] Y.-Y. Zheng and W. Wú, $s_{\pm}$-wave superconductivity in the bilayer two-orbital Hubbard model, Phys. Rev. B **111**, 035108 (2025).

[100] C. Xia, H. Liu, S. Zhou, and H. Chen, Sensitive dependence of pairing symmetry on Ni-e_g crystal field splitting in the nickelate superconductor $La_3Ni_2O_7$, Nat. Commun. **16**, 1054 (2025).

[101] Y. Wang, Z. Chen, Y. Zhang, K. Jiang, and J. Hu, The mottness and the Anderson localization in bilayer Nickelate $La_3Ni_2O_{7-\delta}$, arXiv:2501.08536.

[102] T. Kaneko, M. Kakoi, and K. Kuroki, t-J Model for strongly correlated two-orbital systems: Application to bilayer nickelate superconductors, Phys. Rev. B **112**, 075143 (2025).

[103] H. Shi, Z. Huo, G. Li, H. Ma, T. Cui, D.-X. Yao, and D. Duan, The effect of carrier doping and thickness on the electronic structures of $La_3Ni_2O_7$ thin films, arXiv:2502.04255.

[104] E. K. Ko, Y. Yu, Y. Liu, L. Bhatt, J. Li, V. Thampy, C.-T. Kuo, B. Y. Wang, Y. Lee, K. Lee, J.-S. Lee, B. H. Goodge, D. A. Muller, and H. Y. Hwang, Signatures of ambient pressure superconductivity in thin film $La_3Ni_2O_7$, Nature (London) **638**, 935 (2025).

[105] G. Zhou, W. Lv, H. Wang, Z. Nie, Y. Chen, Y. Li, H. Huang, W. Chen, Y.-J. Sun, Q.-K. Xue, and Z. Chen, Ambient-pressure superconductivity onset above 40 K in $(La,Pr)_3Ni_2O_7$ films, Nature (London) **640**, 641 (2025).

[106] B. Geisler, J. J. Hamlin, G. R. Stewart, R. G. Hennig, and P. Hirschfeld, Fermi surface reconstruction in strained $La_3Ni_2O_7$ on $LaAlO_3$(001) and $SrTiO_3$(001), arXiv:2411.14600.

[107] Y. Liu, E. K. Ko, Y. Tarn, L. Bhatt, B. H. Goodge, D. A. Muller, S. Raghu, Y. Yu, and H. Y. Hwang, Superconductivity and normal-state transport in compressively strained $La_2PrNi_2O_7$ thin films, Nat. Mater. **24**, 1221 (2025).

[108] L. Bhatt, A. Y. Jiang, E. K. Ko, N. Schnitzer, G. A. Pan, D. F. Segedin, Y. Liu, Y. Yu, Y.-F. Zhao, E. A. Morales, C. M. Brooks, A. S. Botana, H. Y. Hwang, J. A. Mundy, D. A. Muller, and B. H. Goodge, Resolving structural origins for superconductivity in strain-engineered $La_3Ni_2O_7$ thin films, arXiv:2501.08204.

[109] C. Yue, J.-J. Miao, H. Huang, Y. Hua, P. Li, Y. Li, G. Zhou, W. Lv, Q. Yang, H. Sun, Y.-J. Sun, J. Lin, Q.-K. Xue, Z. Chen, and W.-Q. Chen, Correlated electronic structures and unconventional superconductivity in bilayer nickelate heterostructures, Natl. Sci. Rev. **12**, nwaf253 (2025).

[110] Z.-Y. Shao, Y.-B. Liu, M. Liu, and F. Yang, Band structure and pairing nature of $La_3Ni_2O_7$ thin film at ambient pressure, Phys. Rev. B **112**, 024506 (2025).

[111] X. Hu, W. Qiu, C.-Q. Chen, Z. Luo, and D.-X. Yao, Electronic structures and multi-orbital models of $La_3Ni_2O_7$thin films, arXiv:2503.17223.

[112] C. Tsuei and J. Kirtley, Pairing symmetry in cuprate superconductors, Rev. Mod. Phys. **72**, 969 (2000).

[113] P. A. Lee, N. Nagaosa, and X.-G. Wen, Doping a mott insulator: Physics of high-temperature superconductivity, Rev. Mod. Phys. **78**, 17 (2006).

[114] L. Taillefer, Scattering and pairing in cuprate superconductors, Annu. Rev. Condens. Matter Phys. **1**, 51 (2010).

[115] C. Proust and L. Taillefer, The remarkable underlying ground states of cuprate superconductors, Annu. Rev. Condens. Matter Phys. **10**, 409 (2019).

[116] A. S. Botana and M. R. Norman, Similarities and differences between $LaNiO_2$ and $CaCuO_2$ and implications for superconductivity, Phys. Rev. X **10**, 011024 (2020).

[117] H. Bhatta, X. Zhang, Y. Zhong, and C. Jia, Structural and electronic evolution of bilayer nickelates under biaxial strain, arXiv:2502.01624.

[118] F. C. Zhang and T. M. Rice, Effective Hamiltonian for the superconducting Cu oxides, Phys. Rev. B **37**, 3759 (1988).

[119] D. Li, K. Lee, B. Y. Wang, M. Osada, S. Crossley, H. R. Lee, Y. Cui, Y. Hikita, and H. Y. Hwang, Superconductivity in an infinite-layer nickelate, Nature (London) **572**, 624 (2019).

[120] Y. Nomura and R. Arita, Superconductivity in infinite-layer nickelates, Rep. Prog. Phys. **85**, 052501 (2022).

[121] B. Y. Wang, K. Lee, and B. H. Goodge, Experimental progress in superconducting nickelates, Annu. Rev. Condens. Matter Phys. **15**, 305 (2024).

[122] G. Kotliar and J. Liu, Superexchange mechanism and d-wave superconductivity, Phys. Rev. B **38**, 5142 (1988).

[123] S. R. White, Density-matrix algorithms for quantum renormalization groups, Phys. Rev. B **48**, 10345 (1993).

[124] Y. L. Lee, Y. W. Lee, C.-Y. Mou, and Z. Y. Weng, Two-leg t-j ladder: A mean-field description, Phys. Rev. B **60**, 13418 (1999).

[125] C. Castellani, C. R. Natoli, and J. Ranninger, Magnetic structure of V_2O_3 in the insulating phase, Phys. Rev. B **18**, 4945 (1978).

[126] M. Tinkham, *Introduction to Superconductivity* (Courier Corporation, 2004).

[127] J. Haegeman and L. Devos, Jutho/TensorKit.jl: v0.12.7 (v0.12.7) (2024), Zenodo, https://doi.org/10.5281/zenodo.13950435.

[128] Q.-Y. Li, Qiaoyi-Li/FiniteMPS.jl: v1.6.1 (v1.6.1), (2025), Zenodo, https://doi.org/10.5281/zenodo.14615184.

[129] A. Weichselbaum, Non-abelian symmetries in tensor networks: A quantum symmetry space approach, Ann. Phys. **327**, 2972 (2012).

[130] A. Weichselbaum, X-symbols for non-abelian symmetries in tensor networks, Phys. Rev. Res. **2**, 023385 (2020).

[131] A. Luther and V. J. Emery, Backward scattering in the one-dimensional electron gas, Phys. Rev. Lett. **33**, 589 (1974).